Highly Tunable Nonlinear Hall Effects Induced by Spin-Orbit Couplings in Strained Polar Transition-Metal Dichalcogenides

Benjamin T. Zhou,[*,‡] Cheng-Ping Zhang,[‡] and K.T. Law[†]

Department of Physics, Hong Kong University of Science and Technology, Clear Water Bay, Hong Kong, China

Recently, signatures of nonlinear Hall effects induced by Berry-curvature dipoles have been found in atomically thin $1T'/T_d$-WTe$_2$. In this paper, we show that in strained polar transition-metal dichalcogenides (TMDs) with $2H$ structures, Berry-curvature dipoles created by spin degrees of freedom lead to strong nonlinear Hall effects. Under an easily accessible uniaxial strain of order 0.2%, strong nonlinear Hall signals, characterized by a Berry-curvature dipole on the order of 1 Å, arise in electron-doped polar TMDs such as MoSSe, and this is easily detectable experimentally. Moreover, the magnitude and sign of the nonlinear Hall current can be easily tuned by electric gating and strain. These properties can be used to distinguish nonlinear Hall effects from classical mechanisms such as ratchet effects. Importantly, our system provides a potential scheme for building electrically switchable energy-harvesting rectifiers.

I. INTRODUCTION

The study of Hall effects has been one of the central topics in condensed-matter physics [1,2]. Within the linear-response regime, the Hall effect arises only when time-reversal symmetry is broken [3,4]. Recently, however, it was proposed by Sodemann and Fu [5] that Hall effects can occur in a wide class of time-reversal-invariant materials with broken spatial inversion symmetry. In such systems, the total Berry flux over the equilibrium distribution is zero due to time-reversal symmetry [1], while Berry curvatures can emerge locally in the Brillouin zone, with counterpropagating charge carriers having different Berry curvatures. Under an applied electric field, the current-carrying state maintains an imbalance between counterpropagating carriers, which results in a nonzero Berry-curvature flux under proper symmetry conditions [6]. This leads to anomalous Hall currents, which establish a Hall voltage in the steady state. As the electric field plays both the role of driving the system out of equilibrium and that of inducing anomalous velocities, the Hall current scales quadratically with the voltage bias. This special type of Hall effect is thus referred to as the nonlinear Hall effect (NHE). Because of the nonlinear current response, the NHE can convert oscillating electric fields into dc currents, a process known as rectification, which has potential applications for next-generation wireless and energy-harvesting devices [7].

The nonlinear Hall response is characterized by the first-order moment of the Berry curvatures over occupied states [5,8,9], called the Berry-curvature dipole. In two-dimensional (2D) systems, the Berry-curvature dipole transforms as a pseudovector, and thus the maximum symmetry allowed for a nonzero moment is a single mirror symmetry (a mirror plane perpendicular to the 2D plane). Interestingly, atomically thin transition-metal dichalcogenides (TMDs) with a $1T'/T_d$ structure, such as MoTe$_2$ and WTe$_2$, have a single in-plane mirror symmetry [10], and nonzero Berry-curvature dipoles have been proposed to exist in these materials [11,12]. Remarkably, two recent experiments have independently observed signatures of Hall effects in bilayer [13] and multilayer WTe$_2$ [14] in the absence of magnetic fields. Importantly, a quadratic scaling relation was found between the transverse voltage and the applied source-drain bias. While the observations are consistent with NHEs induced by Berry-curvature dipoles [15], due to the relatively weak gate dependence of Berry-curvature dipoles in WTe$_2$ [13], it remains experimentally challenging to directly rule out alternative trivial interpretations such as electron ratchet effects [5,14,16].

Besides $1T'/T_d$ TMDs, it is known that TMDs with the usual $2H$ structure also possess nontrivial Berry curvatures due to intrinsically broken inversion in the orbital degrees of freedom [17,18]. However, the threefold (C_3) symmetry in $2H$ TMDs forces the Berry-curvature dipole to vanish [5]. Under applied strains that break the C_3 symmetry, nonzero Berry-curvature dipoles can arise in $2H$ TMDs [5,6,11]. Unfortunately, the dipole moment in strained conventional $2H$ TMDs has been shown to be weak (on the order of 0.01 Å) [5,11], mainly due to the

---

[*]bentzhou@ust.hk
[†]phlaw@ust.hk
[‡]These authors contributed equally to this work.

024053-1

weak Berry curvatures generated by the huge Dirac mass (on the order of 1 eV) in the orbital degrees of freedom [17].

Lately, it has been proposed that in gated [19] or polar [20,21] $2H$ TMDs, the combined effects of Rashba and Ising spin-orbit couplings (SOCs) result in a different type of Berry curvature in the spin degrees of freedom [22,23]. Importantly, in $2H$ TMDs the SOC-induced effect was found to be strong, and this dominates over the conventional orbital effect and significantly changes the Berry curvatures in $2H$ TMDs. However, the role of these SOC-induced Berry curvatures in creating nonlinear Hall effects in $2H$ TMDs remains unknown.

In this paper, we show that the large Berry curvatures induced by SOCs lead to strong gate-tunable nonlinear Hall effects in molybdenum-based polar $2H$ TMDs (Fig. 1) such as MoSSe [24,25]. With an easily accessible low carrier density and a weak uniaxial strain of order 0.2%, pronounced nonlinear Hall signals arise in polar TMDs, characterized by Berry-curvature dipoles on the order of 1 Å (Fig. 3), comparable to the optimal values observed recently in $1T_d$-WTe$_2$ [13,14].

Importantly, the magnitude and sign of the nonlinear Hall signals in strained polar TMDs change dramatically upon gating of the Fermi level by 10–20 meV away from the conduction-band minimum [Fig. 2(c)]. Therefore, nonlinear Hall effects in strained polar TMDs generally exhibit a stronger gate dependence than does $1T'/T_d$-WTe$_2$ [13], which can be easily detected in Hall measurements
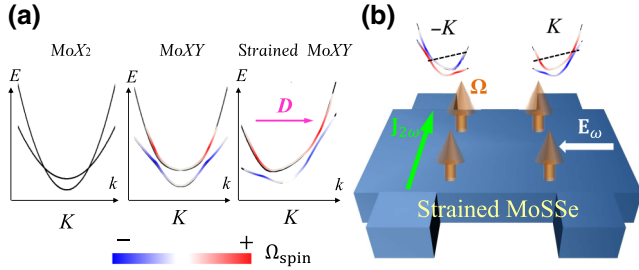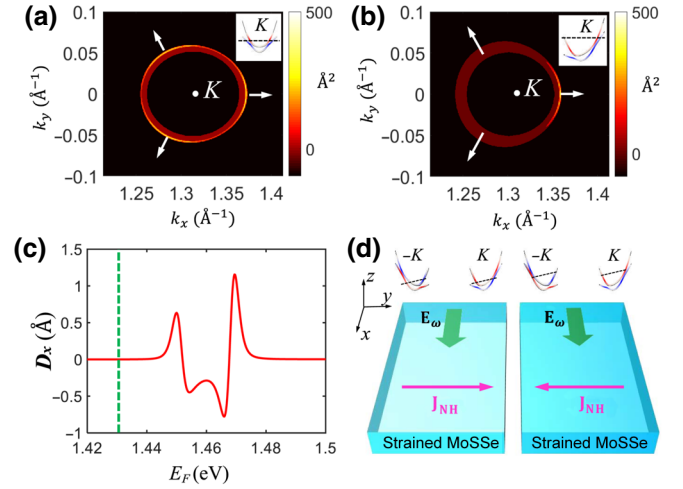

FIG. 2. Realistic Berry curvature and its dipole moment in MoSSe. Berry-curvature profiles on the Fermi-surface contour in (a) unstrained MoSSe, and (b) strained MoSSe. Contributions from both spin subbands are included. The Berry curvatures are weighted by the normalized delta function $\delta_F/\delta_F^{\max}$, with temperature $T = 10$ K. Insets in (a),(b): schematic illustrations of locations of E_F in each case. The colors of the bands indicate the values of the Berry curvature. (c) Berry-curvature dipole D_x versus Fermi energy E_F in strained MoSSe (red solid line) calculated from realistic tight-binding model under uniaxial strain $u_{xx} = 4\%$. The green dashed line indicates the location of the band minimum. (d) Schematic illustration of strong gate dependence of nonlinear Hall effects in strained MoSSe. When E_F is gated across the band anticrossing associated with the right-movers in the $+K$-valley, the nonlinear Hall current $\mathbf{J}_{\mathrm{NH}}$ switches sign.

with moderate gating. We point out further that the gate-sensitive NHE in strained polar TMDs provides a promising scheme for realizing electrically switchable rectifiers for wireless energy-harvesting devices. The highly gate-tunable NHE in strained polar TMDs also serves as a distinctive and accessible experimental signature of Berry-curvature dipoles, which can be distinguished from nonlinear effects due to trivial classical mechanisms [5,14,16].

II. RESULTS

A. Effective model Hamiltonian for strained MoSSe

Throughout this paper, we consider MoSSe as a specific example of a polar TMD; it has been successfully fabricated in recent experiments [24,25]. However, our predictions apply generally to the whole class of molybdenum-based polar TMDs MoXY ($X \neq Y$) [20,21].

To distinguish the two types of Berry curvature in $2H$ TMDs originating from orbital (spin) degrees of freedom, we use the notation Ω_{orb} (Ω_{spin}) to denote the conventional Berry curvature (SOC-induced Berry curvature).

FIG. 1. Schematic illustration of Berry-curvature dipole in strained molybdenum-based transition-metal dichalcogenides. (a) Ω_{spin} near the conduction-band minimum (CBM) at the $+K$-point in a $2H$ TMD. Left panel: in MoX_2, spin-up and spin-down bands cross at finite momentum. Ω_{spin} is zero due to the absence of Rashba SOCs. Middle panel: in MoXY, Rashba SOCs cause anticrossings within two spin subbands, where hot spots of Ω_{spin} emerge at the same energy for left-movers and right-movers. Right panel: with $u_{xx} \neq 0$, the anticrossings for left-movers and right-movers are separated, creating a nonzero Berry-curvature dipole $\mathbf{D}$ in MoXY. (b) Under an electric field $\mathbf{E}_\omega$ with frequency ω, the nonequilibrium state in strained MoSSe gains a net Berry-curvature flux (denoted by the orange arrows), which combines with $\mathbf{E}_\omega$ to generate a nonlinear Hall current signified by a second-harmonic component $\mathbf{J}_{2\omega}$.

To describe the essential mechanism behind the emergence of the Berry-curvature dipole, we first construct an effective Hamiltonian for n-type (electron-doped) strained polar TMDs. The crystal structure of a generic polar TMD is almost the same as that of the usual $2H$ TMD except that the triangularly arranged transition-metal atoms (M) are sandwiched between two different layers of chalcogen atoms [20,21,24,25]. Thus, the out-of-plane mirror symmetry (mirror plane parallel to the 2D plane of M atoms), which is generally respected by the usual $2H$ TMDs, is intrinsically broken. The resultant symmetry group of MoSSe is the product group of the C_{3v} point group and time-reversal symmetry $\mathcal{T}$.

Near the conduction-band minimum at the K-points, the electrons in polar TMDs originate predominantly from the d_{z^2} orbitals of the M atoms [26]. In the basis formed by the spins of d_{z^2} electrons, the unstrained effective Hamiltonian of MoSSe can be written as [22,23,27]

$$H_0 = \xi_{\mathbf{k}}\sigma_0 + \alpha_{\mathrm{SO}}(k_y\sigma_x - k_x\sigma_y) + \epsilon\beta_{\mathrm{SO}}(\mathbf{k})\sigma_z. \quad (1)$$

Here, $\sigma_i, i = 0, x, y, z$, denotes the usual Pauli matrices acting on the spin degrees of freedom. $\xi_{\mathbf{k}} = |\mathbf{k}|^2/2m^* - \mu$ denotes the kinetic-energy term, m^* is the effective mass of the electron band, μ is the chemical potential, and $\epsilon = \pm$ is the valley index.

The $\beta_{\mathrm{SO}}(\mathbf{k})$ term refers to the Ising SOC, which originates from the atomic spin-orbit coupling, as well as to the breaking of an in-plane mirror symmetry [28–31]. In previous studies on $2H$ TMDs, the Ising SOC was usually treated as a constant near the K-points [22,23,27]. However, in realistic band structures of conventional molybdenum-based $2H$ TMDs, the spin-up and spin-down bands cross at a finite momentum k_0 [left panel of Fig. 1(a)] [26]. This indicates a sign change in the Ising SOC term at the crossing, which can be accounted for by quadratic corrections in $\mathbf{k}$: $\beta_{\mathrm{SO}}(\mathbf{k}) = \beta_0 + \beta_1 k^2$, with $\mathrm{sgn}(\beta_0)\mathrm{sgn}(\beta_1) < 0$. The crossings for the spin-up and spin-down bands occur at $k_0 = \pm\sqrt{-\beta_0/\beta_1}$. The α_{SO} term is known as the Rashba SOC [32], and arises in MoSSe due to the intrinsically broken out-of-plane mirror symmetry.

Interestingly, for each K-valley, the coexistence of Ising and Rashba SOCs results in a modified massive Dirac Hamiltonian $H_0 = \xi_{\mathbf{k}}\sigma_0 + \mathbf{d}_\epsilon(\mathbf{k}) \cdot \boldsymbol{\sigma}$, which is reminiscent of the well-known BHZ model for a 2D topological insulator [33], with $\mathbf{d}_\epsilon(\mathbf{k}) = [\alpha_{\mathrm{SO}}k_y, -\alpha_{\mathrm{SO}}k_x, \epsilon(\beta_0 + \beta_1 k^2)]$, except that the kinetic $\xi_{\mathbf{k}}$ term bends the electron bands up, with two nondegenerate spin subbands [Fig. 1(a)]. The energy spectra for the upper and lower spin subbands are given by $E_\pm(\mathbf{k} + \epsilon\mathbf{K}) = \xi_{\mathbf{k}} \pm \epsilon|\mathbf{d}(\mathbf{k})|$, where

$|\mathbf{d}(\mathbf{k})| = \sqrt{\alpha_{\mathrm{SO}}^2 k^2 + (\beta_0 + \beta_1 k^2)^2}$. The Berry curvatures of the two subbands are given by [34,35]

$$\Omega_{\mathrm{spin},\pm}(\mathbf{k} + \epsilon\mathbf{K}) = \mp\frac{1}{2}\hat{\mathbf{d}}_\epsilon(\mathbf{k}) \cdot \left(\frac{\partial\hat{\mathbf{d}}_\epsilon}{\partial k_x} \times \frac{\partial\hat{\mathbf{d}}_\epsilon}{\partial k_y}\right)$$
$$= \mp\frac{1}{2}\epsilon\frac{\alpha_{\mathrm{SO}}^2(\beta_0 - \beta_1 k^2)}{|\mathbf{d}(\mathbf{k})|^3}. \quad (2)$$

Note that a nontrivial $\Omega_{\mathrm{spin},\pm}(\mathbf{k})$ requires the presence of both Ising and Rashba SOCs. In the absence of Rashba SOCs, the upper and lower subbands consist of decoupled spin-up and spin-down states, and no Ω_{spin} can be generated [left panel of Fig. 1(a)]. In molybdenum-based polar TMDs, the Rashba SOC hybridizes the spin-up and spin-down bands and causes an anticrossing within the spin subbands [middle panel of Fig. 1(a)]. In particular, hot spots of Ω_{spin} emerge in the vicinity of the crossing points k_0, with their signs being opposite in the upper and lower subbands. Given realistic parameters, Ω_{spin} near its hot spots has a magnitude $|\Omega_{\mathrm{spin}}| \gg 100\,\text{Å}^2$ (see Appendix A for details).

Despite the large Ω_{spin}, the Berry-curvature dipole remains zero in unstrained MoSSe due to the threefold (C_3) symmetry [5]. Physically, the Berry-curvature dipole measures the gain in the total Berry-curvature flux in the current-carrying state [6]. When C_3 symmetry is present, the Berry flux from left-movers is always equal to that from right-movers on the Fermi surface [middle panel of Fig. 1(a)]. Thus, the imbalance between left-movers and right-movers established by a source-drain bias leads to no gain in total Berry flux up to the lowest-order correction.

To break the C_3 symmetry, one feasible way is to introduce uniaxial strains [5,6,11]. Following the scheme developed in recent work [36], the effects of strains in 2D TMDs can be modeled by classifying the strain-field tensor $\overleftrightarrow{\mathbf{u}}_{ij} = (\partial_i u_j + \partial_j u_i)/2$ $(i, j = x, y)$ according to the irreducible representations of the C_{3v} point group of polar TMDs. In total, $\overleftrightarrow{\mathbf{u}}$ has three effective independent components: the trace scalar $u_0 \equiv (u_{xx} + u_{yy})$, and the doublet $\{u_1, u_2\} \equiv \{2u_{xy}, u_{xx} - u_{yy}\}$, which transforms as a polar vector. Details of the symmetry properties of u_0, u_1, u_2 are presented in Appendix A.

To capture the essential physics, we consider the effects of strain on spin-independent terms only, which make no contributions to the Berry curvature. This approximation is based on the observation that the coupling strength between the spin-independent terms and the strain field $\overleftrightarrow{\mathbf{u}}$ has an energy scale on the order of 1 eV [36], which is far greater than spin-orbit couplings, which are on the scale of a few to a few tens of millielectronvolts. Up to linear-order terms in $\mathbf{k}$, the effective strained Hamiltonian compatible with the $C_{3v} \otimes \mathcal{T}$ symmetry group is

given by

$$H_{\text{strain}} = [\gamma u_0 + \epsilon\delta(u_1 k_y - u_2 k_x)]\sigma_0,$$
$$H_{\text{eff}} = H_0 + H_{\text{strain}}, \tag{3}$$

where H_{eff} is the total effective Hamiltonian, and γ, δ are effective strain parameters. Considering uniaxial strains in the x direction, i.e., $u_{xx} \neq 0$ and $u_{xy} = u_{yy} = 0$, the strained energy spectra are given by $E'_\pm(\mathbf{k}) = u_{xx}(\gamma - \epsilon\delta k_x) + \xi_\mathbf{k} \pm |\mathbf{d}_\epsilon(\mathbf{k})|$. Clearly, the δ term breaks the C_3 symmetry by shifting the band minimum along the k_x direction [5]. As a result, the two pairs of Berry-curvature hot spots associated with the left-movers and right-movers are energetically separated [Fig. 1(a), right panel]. For a Fermi level close to one of these separated hot spots, an applied bias in the x direction creates an imbalance between left-movers and right-movers, and the system acquires a nonzero out-of-plane Berry-curvature flux in the current-carrying state [orange arrows in Fig. 1(b)]. This current-induced Berry flux then combines again with the applied field to generate currents in the transverse y direction, as shown schematically in Fig. 1(b).

B. Large gate-tunable Berry-curvature dipoles in strained MoSSe

Having established how Ω_{spin} combines with uniaxial strains to create Berry-curvature dipoles, we now go beyond the effective two-band model and study the nonlinear Hall effect in strained MoSSe in realistic situations. Using a six-orbital tight-binding model for strained TMDs [26,36], we take both Ω_{spin} and Ω_{orb} into account and study the Berry curvature as well as its dipole moment in electron-doped strained MoSSe. As we are about to show, the dominance of Ω_{spin} over Ω_{orb}, together with uniaxial strains, leads to strong and highly gate-tunable nonlinear Hall effects in strained MoSSe. Details of the tight-binding Hamiltonian are presented in Appendices B and C.

As discussed in the last section, the Berry-curvature dipole measures the lowest-order correction to the total-Berry curvature flux in the nonequilibrium state. This physical meaning is revealed by the following formal expression [5,13]:

$$D_\alpha = -\sum_n \int \frac{d^2\mathbf{k}}{(2\pi)^2}(\partial_{k_\alpha} f_n)\Omega_n(\mathbf{k})$$
$$= \sum_n \int \frac{d^2\mathbf{k}}{(2\pi)^2} v_{n,\alpha}(\mathbf{k})\delta_F(E_n - E_F)\Omega_n(\mathbf{k}). \tag{4}$$

Here, D_α denotes the α component of the Berry-curvature dipole $\mathbf{D}$, with $\alpha = x, y$, and f_n, Ω_n refer to the equilibrium

distribution function and Berry curvature of bands indexed by n. $v_{n,\alpha} = \partial E_n/\partial k_\alpha$ is the band velocity, and $\delta_F(E - E_F) = -\partial f/\partial E = \{4k_B T \cosh^2[(E - E_F)/2k_B T]\}^{-1}$ mimics a delta function with its maximum value $\delta_F^{\max} = 1/4k_B T$ centered at E_F.

In general, the Berry-curvature dipole in a polar TMD has contributions from both the K and the $-K$ valley. Because of time-reversal symmetry, $v_{n,\alpha}(\mathbf{k} + \mathbf{K}) = -v_{n,\alpha}(-\mathbf{k} - \mathbf{K})$ and $\Omega_n(\mathbf{k} + \mathbf{K}) = -\Omega_n(-\mathbf{k} - \mathbf{K})$. Thus, the contributions from the two K-valleys are equal, which allows us to consider the $+K$-valley only for simplicity in our following discussions.

As explained previously, the Berry-curvature dipoles vanish in MoSSe in the absence of strain. Since the Berry-curvature dipole is a Fermi-liquid property [5], this symmetry property can be explicitly revealed by the Berry-curvature profile on the Fermi-surface contour of unstrained MoSSe. Without loss of generality, we consider E_F to lie slightly above the Berry-curvature hot spot in the upper band [inset of Fig. 2(a)]. Evidently, due to the C_3 symmetry, the Berry curvatures of threefold-related momentum states $\{\mathbf{k}, C_3\mathbf{k}, C_3^2\mathbf{k}\}$ must satisfy $\Omega_n(\mathbf{k}) = \Omega_n(C_3\mathbf{k}) = \Omega_n(C_3^2\mathbf{k})$ [Fig. 2(a)], and their band velocities [indicated by arrows in Fig. 2(a)] sum to zero: $\sum_{j=1}^3 v_{n,\alpha}(C_3^{j-1}\mathbf{k}) = 0$. These symmetry constraints force the contributions from left-movers and right-movers to cancel each other, leading to vanishing dipole moments in Eq. (4).

However, because the total Berry curvature Ω_{tot} near the band-anticrossing points is approximately the sum of Ω_{spin} and Ω_{orb} (see Appendix D for details), the dominance of Ω_{spin} over Ω_{orb} implies that the behavior of Ω_{tot} is essentially governed by Ω_{spin}. Therefore, Ω_{tot} in both the upper and the lower subbands exhibits similar nonuniform momentum-space profiles to Ω_{spin} (see Appendix D for details), with hot spots emerging near the anticrossing points [shown schematically in the inset of Fig. 2(a)].

Importantly, Ω_{tot} has opposite signs in the upper and lower subbands [22] [indicated by the red and blue colors in the insets of Figs. 2(a) and 2(b)]. While this generally leads to partial cancellation within the two subbands, it is important to note that for a Fermi level located slightly above (below) the anticrossing points, the Fermi momentum of the upper (lower) subband is closer to the hot spots, and thus its contribution to the Berry curvature dominates over the other subband at the Fermi energy, leading to a large net Berry flux for each K-valley on the Fermi-surface contour. For instance, when the Fermi level is slightly above the band anticrossing, the upper subband dominates, with the overall sign of the Berry curvature being positive around K [Fig. 2(a)].

Under a uniaxial strain, the anticrossings associated with the left-movers and right-movers are energetically separated. Thus, for Fermi levels located slightly above or

below one of the separated anticrossing points, there generally exists a huge difference between the Berry-curvature contributions from left-movers and right-movers. To be specific, we plot the Berry-curvature profile on the Fermi-surface contour of strained MoSSe under a strain $u_{xx} = 4\%$, with E_F lying slightly higher than the anticrossing point associated with the right-movers [inset of Fig. 2(b)]. Evidently, the contributions from the right-movers far exceed those from the left-movers, with the overall sign being positive due to the dominance of the upper band [Fig. 2(b)]. In this case, the system gains a large amount of Berry flux as the left-movers(right-movers) are pumped by the voltage bias to the right(left), which signifies a large Berry-curvature dipole.

Moreover, since the upper (lower) subband dominates for Fermi levels above (below) the anticrossing, the net Berry curvature on the Fermi surface changes sign as the Fermi level is gated across these anticrossing points, indicating a sign switch in the Berry-curvature dipole [Eq. (4)]. The Berry-curvature dipole D_x is plotted as a function of E_F for $u_{xx} = 4\%$ in Fig. 2(c). At the band minimum [indicated by the green dashed line in Fig. 2(c)], the Berry-curvature dipole is zero due to the vanishing band velocity. As E_F increases, the anticrossing associated with the left-movers is first accessed. Evidently, D_x changes from positive to negative values as E_F goes across the anticrossing. This gives rise to a peak followed by a dip, as shown in the D_x-E_F curve [for E_F in the range 1.44–1.46 eV in Fig. 2(c)].

By further raising the Fermi level, one reaches the anticrossing associated with the right-movers. However, since the band velocities of right-movers and left-movers are opposite to each other, D_x changes sign in an opposite manner according to Eq. (4), i.e., from negative to positive values as E_F sweeps across the anticrossing. This leads to a dip followed by a peak in the D_x-E_F curve [for E_F in the range 1.46–1.48 eV in Fig. 2(c)].

Consider a strained MoSSe sample with the coordinates defined in Fig. 2(d). An oscillating electric field with frequency ω, $\mathbf{E}_\omega(t) = \mathrm{Re}\{\mathcal{E}_x e^{i\omega t}\}\hat{x}$, in the x direction can drive a second-harmonic transverse current along the y direction in strained MoSSe [Fig. 1(b)], with the current amplitude given by [5]

$$j_y^{2\omega} = -\frac{e^3 \tau \mathcal{E}_x^2}{2(1 + i\omega\tau)} D_x, \qquad (5)$$

where τ is the relaxation time. As $j_y^{2\omega}$ is proportional to D_x, the nonlinear Hall current in MoSSe also changes sign upon gating of the Fermi level across the anticrossing. This sign switch occurs within a narrow Fermi-level range $\Delta E_F \sim 10$ meV [Fig. 2(d)] and thus can be easily controlled by moderate gating. The second-harmonic Hall current $j_y^{2\omega}$ establishes an ac Hall voltage with frequency 2ω, which can be readily detected by use of the
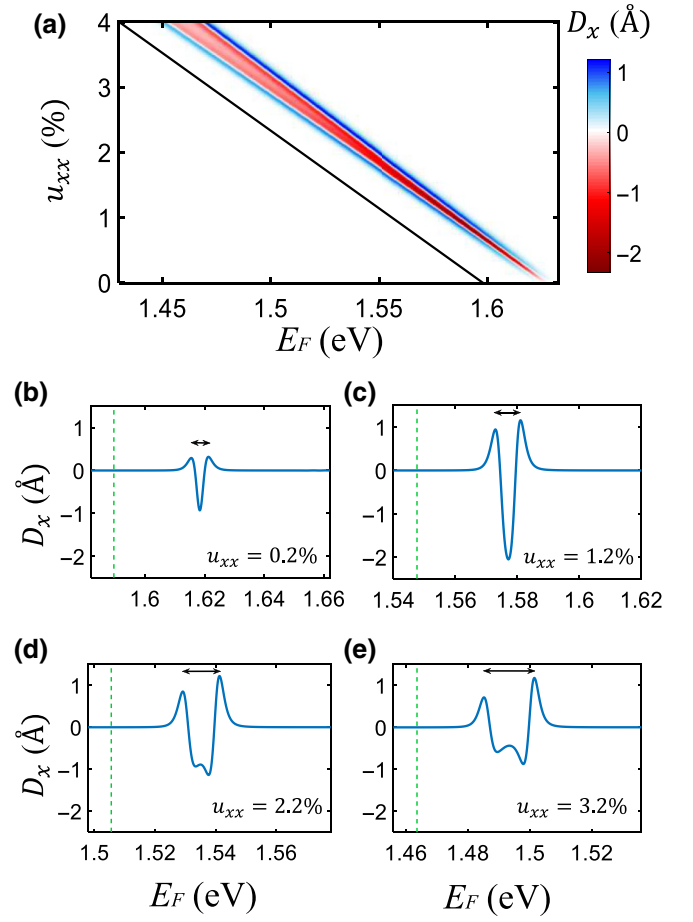

FIG. 3. Evolution of nonlinear Hall signals induced by Berry-curvature dipoles in MoSSe under strains and gating. (a) Strain-gate map of Berry dipole D_x in electron-doped MoSSe. The black solid line indicates the location of the conduction-band minimum. Note that the energy offsets in the CBM upon increasing u_{xx} are due to on-site energy corrections induced by strains (see Appendix C). (b)–(e) Gate dependence of D_x with $u_{xx} = 0.2\%, 1.2\%, 2.2\%, 3.2\%$. The green dashed lines correspond to the location of the CBM in each case. The black double arrows indicate the energy separation between the anticrossings associated with the left-movers and the right-movers near the K-valley.

usual Hall bar geometry as in recent experiments on bilayer and multilayer WTe$_2$ [13,14].

C. Strain-gate map of nonlinear Hall response in MoSSe

In this section, we systematically demonstrate how the gate dependence of NHEs in MoSSe evolves under a uniaxial strain u_{xx} ranging from 0% up to 4% [Fig. 3(a)]. Importantly, we show that a tiny amount of uniaxial strain $u_{xx} \sim 0.2\%$ is sufficient for creating sizable Berry-curvature dipoles of order 1 Å [Fig. 3(b)].

As explained in Sec. II A, the uniaxial strain plays the essential role of breaking the C_3 symmetry and gives rise to nonzero Berry dipoles in MoSSe. In particular, large Berry dipoles in MoSSe are physically established by the strain-induced energy separation of Berry-curvature hot spots associated with left-movers and right-movers [Fig. 1(a)]. Thus, as one gradually turns on the uniaxial strain, the Berry-curvature hot spots associated with left-movers and right-movers start to become separated in energy and a nonzero Berry dipole D_x emerges.

A complete 2D map of D_x as a function of the Fermi energy E_F and uniaxial strain u_{xx} is shown in Fig. 3(a), with the black solid line indicating the locations of the conduction-band minimum. At $u_{xx} = 0\%$, the C_3 symmetry in MoSSe is respected, with $D_x = 0$ in all ranges of E_F. As u_{xx} is turned on, nonzero Berry dipoles D_x start to emerge. Notably, the band-anticrossing points providing Berry-curvature hot spots [Fig. 1(a)] are generically located approximately 20 meV away from the CBM. As E_F accesses these hot spots, it is evident from Fig. 3(a) that pronounced signals in D_x of order 1 Å readily appear under very weak uniaxial strains $u_{xx} \sim 0.2\%$.

To understand why such strong Berry dipoles can be induced by weak strains, we study the evolutionary behavior of D_x under strain by plotting D_x as a function of E_F at various fixed strains $u_{xx} = 0.2\%, 1.2\%, 2.2\%, 3.2\%$, as shown in Figs. 3(b)–3(e). The black double arrows in each case measure the energy separation between the lowest- and highest-lying Berry-curvature hot spots.

As discussed in Sec. II B, under a uniaxial strain as strong as $u_{xx} = 4\%$, the band anticrossings associated with the left-movers and right-movers are unambiguously separated in energy. As the Berry-curvature hot spots are accessed successively, the sign changes in the Berry-curvature hot spots are signified by peak-to-dip and dip-to-peak behaviors in the D_x-E_F curve [Fig. 2(c)].

Notably, one of the two dips in D_x originates from the left-movers in the upper band and the other originates from the right-movers in the lower band, with both their band velocities and their Berry curvatures being opposite to each other. As a result, their contributions to D_x are additive [Eq. (4)]. Upon a decrease in the uniaxial strain, the two dips start to merge with each other, which enhances the total Berry-curvature dipole, which reaches a maximum $D_x \sim 2$ Å for $u_{xx} \sim 1\%$ as shown in Fig. 3(a). With a further decrease in u_{xx}, although the total D_x would ultimately vanish in the zero-strain limit, the additive contributions from the merging of the two dips in D_x remain strong for weak finite strains. In particular, the magnitude of the total D_x is still of order 1 Å for $u_{xx} \sim 0.2\%$, where the merging of the two dips happens [Fig. 3(b)].

It is also worth noting that the special evolutionary behavior of the D_x-E_F curves under strain, particularly the effect of merging of the two dips upon decreasing

the uniaxial strain, provides yet another unique signature of the gate-tunable nonlinear Hall effect in strained MoSSe.

D. Potential gate-tunable high-frequency rectifiers based on strained polar TMDs

In this section, we discuss how the highly tunable NHE in strained polar TMDs provides a potential scheme for switchable high-frequency rectifiers.

In the past decade, rapid developments in wireless technologies have led to an increasing demand for portable microsized devices that can harvest the energy of ambient electromagnetic (EM) radiation. At the heart of these energy harvesters lies the physical process known as rectification, the conversion of oscillating EM fields into dc currents.

While conventional rectifiers based on semiconductor diodes have found a wide range of industrial applications, a fundamental limitation exists on their operating frequencies [37,38]. In particular, for a preferred current direction to be effectively selected, the diode transition time (i.e., the time scale for a p-n junction to enter a complete open-circuit state upon reversing the bias) must be much shorter than the period of the EM waves. The typical diode transition time, on a nanosecond scale, sets the maximum frequency limit within the gigahertz range, and the vast amount of energy stored in terahertz and far-infrared radiation, which has natural sources such as thermal radiation, is hard to harvest with existing rectifiers.

To bypass the frequency threshold, an alternative scheme based on intrinsic nonlinear properties of homogeneous materials was proposed recently [7]. Notably, regardless of the frequency of the applied or ambient ac field, a second-order nonlinearity generically results in a dc response. Thus, the nonlinear Hall effect provides a possible means to build high-frequency rectifiers that can harvest energy from radiation in the terahertz and far-infrared regimes. In particular, the strained polar TMDs studied in this paper can serve as potential electrically switchable high-frequency rectifiers, which control both the amplitude and the direction of rectified currents simply by the use of electric gates.

With the same setup as in Fig. 2(d), apart from the second-harmonic component discussed previously, the nonlinear Hall current $\mathbf{J}_{NH}$ generated by an ac electric field $\mathbf{E}_\omega(t) = \text{Re}\{\mathcal{E}_x e^{i\omega t}\}\hat{x}$ is partially rectified due to the second-order nonlinearity in $\mathcal{E}_x$, with the dc current component given by [5]

$$j_y^0 = -\frac{e^3 \tau |\mathcal{E}_x|^2}{2(1 + i\omega\tau)} D_x. \tag{6}$$

It is clear from Eq. (6) that, via a moderate gate voltage, the amplitude and direction of the rectified current j_y^0 can be regulated in a similar manner to the D_x-E_F curve in

Fig. 2(c). This provides an easy method of charge regulation, which is indispensable for real electronic devices. Thus, strained polar TMDs can be used to build a NHE-based high-frequency rectifier which integrates the generation and regulation of charging dc currents within a single device.

III. DISCUSSION

Here, we discuss several important points about nonlinear Hall effects in strained polar TMDs.

First of all, we point out that while strong spin-orbit interactions have been known to exist in TMD materials for years [17,27], the effect of SOCs has been completely ignored in all previous studies on nonlinear Hall physics in strained $2H$ TMDs [5,11]. In this paper, we point out that SOCs can significantly change the nonlinear Hall physics in $2H$ TMDs.

Particularly, in the usual strained $2H$ TMDs, where Ω_{spin} is absent, the optimal value of D_x due to Ω_{orb} can only be of order 0.01 Å under a rather strong uniaxial strain $u_{xx} = 2\%$ [5,11]. In sharp contrast, due to the Ω_{spin} induced by SOCs, a strong Berry dipole of order 1 Å emerges under a weak uniaxial strain on the order of 0.2% (Fig. 3).

Moreover, the sign of D_x for electron- or hole-doped samples cannot change, due to the fact that the sign of Ω_{orb} is fixed in both the conduction and the valence band [5,11]. On the other hand, as we show explicitly in Fig. 3, the nonlinear Hall current becomes highly tunable by gating and strain due to the special properties of Ω_{spin} induced by SOCs. Thus, our results demonstrate that SOCs change the nonlinear Hall physics in TMDs in a qualitative way. Also, as the Berry dipole due to Ω_{orb} never changes sign, the sign-changing nonlinear Hall current in strained polar TMDs provides a distinctive electrical signature of the recently discovered Berry curvature Ω_{spin} derived from spin degrees of freedom.

It is important to note that that the NHEs in strained polar TMDs generally have a much stronger gate dependence than in $1T_d$-WTe$_2$. The strong gate dependence of the NHEs not only provides a practical way to realize gate-tunable Hall devices, but also serves as a distinctive signature of the nontrivial origin of the Berry phase. In particular, a gate-sensitive nonlinear Hall signal due to Berry-curvature dipoles can be distinguished from trivial mechanisms, such as ratchet effects [5,14,16], that are much less sensitive to gating.

In a recent experiment on bilayer $1T'$-WTe$_2$, the sign of the Berry-curvature dipole D_x was generally fixed in the neighborhood of the charge-neutrality point near the band edges [13]. To switch the sign of D_x, one generally needs to gate the Fermi level to at least 50–100 meV away from the band edges, which requires a rather strong gating field. Furthermore, without a dual-gate setup, such a strong gating field inevitably introduces out-of-plane displacement

fields that cause complications in the band structure as well as Berry-curvature effects [13]. To unambiguously identify the Berry-phase origin of nonlinear Hall effects in $1T_d$-WTe$_2$, a dual-gate setup is necessary to control the carrier density and the displacement field independently.

In contrast, the Berry-curvature dipole in strained polar TMDs can switch its sign dramatically within a narrow Fermi-level range $\Delta E_F \sim 10$–20 meV. This range can be easily achieved by moderate gating, which has been accessed in previous gating experiments on normal $2H$ TMDs [39]. Moreover, the strong gate dependence of D_x in strained polar TMDs occurs for a Fermi level approximately 20 meV measured from the conduction-band edge. This corresponds to a relatively low carrier-density regime ($n_{\text{2D}} \sim 1 \times 10^{12}$ cm^{-2}), which has also been readily accessed by weak gating [39,40] without introducing a significant displacement field. Thus, a dual-gate setup is not necessary for detecting the gate dependence of D_x in strained polar TMDs, and we expect gate-tunable NHEs in strained polar TMDs to be much more easily observed experimentally than in $1T_d$-WTe$_2$.

Besides, the large magnitude and strong gate-tunability of the Berry-curvature dipole predicted in this paper originate from the intrinsic band anticrossings caused by Ising and Rashba SOCs in molybdenum-based polar TMDs. They do not require any further experimental design apart from the strain. To demonstrate the generality of our predictions, we present the gate dependence of nonlinear Hall signals in another molybdenum-based polar TMD, MoSeTe, in Appendix E. The same qualitative features as in Fig. 3 are found in the D_x-E_F curve for strained MoSeTe.

Also, as long as the C_3 symmetry is broken, the details of the strain configuration do not affect our predictions qualitatively. We point out further that for any strain configuration satisfying $u_{xy} = 0$ and $u_{xx} \neq u_{yy}$, the in-plane mirror symmetry $x \mapsto -x$ is preserved in strained MoSSe, with its point group being identical to that of bilayer and multilayer $1T_d$-WTe$_2$ [10,13]. Thus, the Berry-curvature dipole has only a nonzero x component D_x, which is perpendicular to the mirror plane. In this case, nonlinear Hall effects can be observed as long as the applied electric field deviates from the mirror-invariant y axis, as demonstrated in a recent experiment on multilayer $1T_d$-WTe$_2$ by Kang *et al.* [14].

In addition, it was shown previously that Ω_{spin} also arises in tungsten-based TMDs [22]. However, due to the absence of band anticrossings driven by SOCs in W-based materials, the Berry curvature has a much less nonuniform profile than in the molybdenum-based case, and the nonlinear Hall effect in W-based polar TMDs is much weaker. Detailed discussions of W-based polar TMDs are presented in Appendix E.

We note parenthetically that, while a few recent publications have pointed out possible extrinsic contributions to nonlinear Hall effects due to disorder scattering [41–44],

it has been suggested that the total nonlinear Hall conductivity remains proportional to the Berry-curvature dipole in general [42,43]. In particular, a recent experiment on bilayer $1T'$-WTe$_2$ has unambiguously demonstrated that the sign of the total nonlinear Hall current is almost strictly controlled by the Berry-curvature dipole [13]. Thus, we believe that the qualitative features of NHEs in polar TMDs predicted in this paper will not be affected by extrinsic effects.

Last but not least, for p-type polar TMDs, the effect of Ω_{spin} is almost negligible near the K-points due to the strong Ising SOC on the order of 100 meV in the valence band [26], and the total Berry curvature is dominated by the conventional Ω_{orb} [22]. Thus, for hole-doped polar TMDs, one expects the Berry-curvature dipole to be very weak, similarly to the case in conventional $2H$ TMDs as studied in previous work [5,11].

ACKNOWLEDGMENTS

APPENDIX A: EFFECTIVE HAMILTONIAN FOR STRAINED MoSSe

Here, we derive the effective Hamiltonian near the conduction-band minimum for MoSSe by group theory. In the absence of strain, the electronic bands near the conduction-band minimum at the K-points are dominated by the d_{z^2} orbitals, with spin degrees of freedom. As mentioned in the main text, the symmetry group of MoSSe is given by the product group $C_{3v} \otimes \mathcal{T}$, with the following generators: (i) a threefold rotation ($\hat{C}_3$), (ii) a mirror reflection ($\hat{M}_x$), and (iii) a time reversal $\mathcal{T}$. The valley index, momentum, and spin transform under these generators as follows:

$$\hat{C}_3 : \epsilon \mapsto \epsilon, k_{\pm} \mapsto e^{\pm i 2\pi/3} k_{\pm},$$
$$\sigma_{\pm} \mapsto e^{\pm i 2\pi/3} \sigma_{\pm}, \sigma_z \mapsto \sigma_z,$$
$$\hat{M}_x : \epsilon \mapsto -\epsilon, k_+ \leftrightarrow -k_-, \sigma_+ \mapsto \sigma_-, \sigma_z \mapsto -\sigma_z,$$
$$\mathcal{T} : \epsilon \mapsto -\epsilon, k_+ \mapsto -k_-, \sigma_+ \mapsto -\sigma_-, \sigma_z \mapsto -\sigma_z, \quad \text{(A1)}$$

where $\epsilon = \pm$ is the valley index, $k_{\pm} = k_x \pm i k_y$, and $\sigma_{\pm} = \sigma_x \pm i\sigma_y$. The unstrained Hamiltonian $H_0(\mathbf{k})$, which is invariant under the transformations in Eq. (A1), has the form (up to second order in $\mathbf{k}$)

$$H_0(\mathbf{k} + \epsilon \mathbf{K}) = \xi_{\mathbf{k}}\sigma_0 + \epsilon\beta_{\mathrm{SO}}(\mathbf{k})\sigma_z + \alpha_{\mathrm{SO}}(k_y\sigma_x - k_x\sigma_y).$$
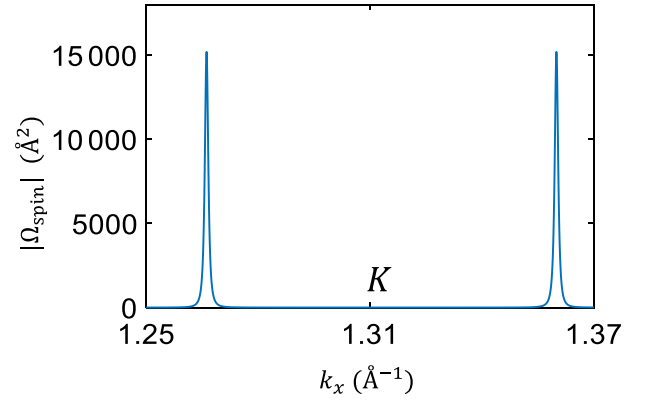$$\text{(A2)}$$

FIG. 4. Magnitude of Berry curvature generated by Ising and Rashba spin-orbit couplings near the K-point in unstrained MoSSe. The coordinate of the K-point is given by $\mathbf{K} = (4\pi/3a, 0) \approx (1.313, 0)$ with $a = 3.19$ Å. Given the effective parameters in Table II, the values of Ω_{orb} are calculated based on Eqs. (1) and (2). Evidently, a huge Ω_{spin} arises in the neighborhood of the band-anticrossing points k_0, with its magnitude generally far greater than 100 Å^2.

Here $\xi_{\mathbf{k}} = k^2/2m^* - \mu$ is the usual kinetic term, $\beta_{\mathrm{SO}}(\mathbf{k}) = \beta_0 + \beta_1 k^2$ is the Ising SOC term with $\beta_0\beta_1 < 0$, and α_{SO} is the strength of the Rashba SOC. As discussed in the main text, in the absence of a Rashba SOC, the spin subbands cross each other at $k_0 = \pm\sqrt{\beta_0/\beta_1}$. When the Rashba SOC is turned on, nontrivial Berry curvatures arise near the K-point as shown in Fig. 4, with their magnitude being huge in the neighborhood of k_0.

Next, we consider correction terms due to strain. According to Ref. [36], general strain effects in two-dimensional crystalline solids are mathematically described by a displacement field $\mathbf{u}(x,y)$ due to distortions in the atomic sites in the strained lattice. In particular, the physical effects of strains are described by the gradients of $\mathbf{u}(x,y)$, $\partial_i u_j$, $(i, j = x, y)$, which form a second-rank tensor. The four independent components of $\partial_i u_j$ can be classified according to the irreducible representations of C_{3v}: (i) the trace scalar $\partial_x u_x + \partial_y u_y$, which forms the trivial (A_1) representation of C_{3v}; (ii) the curl (rotation) of $\mathbf{u}$, $\overleftrightarrow{\boldsymbol{\omega}}_{ij} = \partial_i u_j - \partial_j u_i$, which forms the A_2-representation of C_{3v} (this describes a rotation of the system about the principal z axis under the strain, which can always be taken away by redefining the coordinates); and (iii) the symmetric traceless tensor, $\overleftrightarrow{\boldsymbol{\epsilon}}_{ij} = \frac{1}{2}[\partial_i u_j + \partial_j u_i - (\boldsymbol{\nabla} \cdot \mathbf{u})\delta_{ij}]$, which is characterized by a doublet $\{\partial_x u_y + \partial_y u_x, u_{xx} - u_{yy}\}$ that forms the two-dimensional E-representation of C_{3v}.

To get rid of the redundant rotational part $\overleftrightarrow{\boldsymbol{\omega}}$, the symmetric strain-field tensor $\overleftrightarrow{\mathbf{u}}_{ij} = \frac{1}{2}(\partial_i u_j + \partial_j u_i)$ is introduced, such that the strain effects are essentially captured by the independent components of $\overleftrightarrow{\mathbf{u}}$. Explicitly, under a group element $\hat{g}$, the trace $\partial_x u_x + \partial_y u_y \equiv u_{xx} + u_{yy}$ remains invariant, while the doublet $\{\partial_x u_y + \partial_y u_x, u_{xx} -$

TABLE I. Irreducible representations (IRs) of valley-index, momentum, spin, and strain-tensor components in C_{3v} and parity under time-reversal $\mathcal{T}$.

Basis functions	IR	$\mathcal{T}$
ϵ	A_2	$-$
$1, k_x^2 + k_y^2$	A_1	$+$
$\{k_x, k_y\}$	E	$-$
σ_0	A_1	$+$
σ_z	A_2	$-$
$\{\sigma_x, \sigma_y\}$	E	$-$
u_0	A_1	$+$
$\{u_1, u_2\}$	E	$+$

$u_{yy}\} \equiv \{2u_{xy}, u_{xx} - u_{yy}\} \equiv \{u_1, u_2\}$ transforms as a polar vector:

$$\hat{g} : \{u_1, u_2\} \mapsto \{u_1, u_2\}[D^{(E)}(\hat{g})]^T, \qquad (A3)$$

where $D^{(E)}(\hat{g})$ denotes the representation matrix for $\hat{g}$ in spatial coordinates: $D_{ij}^{(E)}(\hat{g}) = \mathbf{e}_i \cdot \hat{g}\mathbf{e}_j$ $(i,j = x,y)$. Particularly, for the generators $\hat{C}_{3z}, \hat{M}_x$, the representation matrices are

$$D^{(E)}(\hat{C}_{3z}) = \begin{pmatrix} -\dfrac{1}{2} & -\dfrac{\sqrt{3}}{2} \\ \dfrac{\sqrt{3}}{2} & \dfrac{1}{2} \end{pmatrix},$$
$$D^{(E)}(\hat{M}_x) = \begin{pmatrix} -1 & 0 \\ 0 & 1 \end{pmatrix}. \qquad (A4)$$

To sum up the symmetry properties of the physical quantities mentioned above, the irreducible representations of the valley index, momentum, spin, and strain-tensor components are presented in Table I.

In the presence of the strain-field tensor $\overleftrightarrow{\mathbf{u}}$, the underlying point-group symmetries in C_{3v} are manifested by the following equivalence: given any $\hat{g} \in C_{3v}$, after being transformed by $\hat{g}$, a system with the strain $\overleftrightarrow{\mathbf{u}}$ is identical to a system with the transformed strain $\overleftrightarrow{\mathbf{u}}' = \hat{g}\overleftrightarrow{\mathbf{u}}$. Here, the components of $\overleftrightarrow{\mathbf{u}}'$ and $\overleftrightarrow{\mathbf{u}}$ are related by $u_0' = u_0, \{u_1', u_2'\} = \{u_1, u_2\}[D^{(E)}(\hat{g})]^T$.

Formally, this can be expressed as

$$\hat{g}\hat{H}(\overleftrightarrow{\mathbf{u}})\hat{g}^{-1} = \hat{H}(\hat{g}\overleftrightarrow{\mathbf{u}}), \qquad (A5)$$

where $\hat{H}(\overleftrightarrow{\mathbf{u}})$ is the total Hamiltonian under the strain $\overleftrightarrow{\mathbf{u}}$. Note that the symmetry relation above is simply a

generalization of the symmetry property of unstrained system with $\overleftrightarrow{\mathbf{u}} = \mathbf{0}$. Particularly, Eq. (A5) implies that the momentum-space Hamiltonian $H(\mathbf{k})$ satisfies

$$U^\dagger(\hat{g})H(\hat{g}\mathbf{k}, \hat{g}\overleftrightarrow{\mathbf{u}})U(\hat{g}) = H(\mathbf{k}, \overleftrightarrow{\mathbf{u}}), \qquad (A6)$$

where $U(\hat{g})$ denotes the matrix for the group operator $\hat{g}$ in the spin basis: $U_{\sigma\sigma'}(\hat{g}) = \langle \sigma | \hat{g} | \sigma' \rangle$, with $\sigma, \sigma' = \uparrow, \downarrow$. Accordingly, up to first order in $\mathbf{k}$, the effects of strain on the spin-independent terms are described by

$$H_{\text{strain}}(\mathbf{k} + \epsilon\mathbf{K}) = [\gamma u_0 + \epsilon\delta(k_y u_1 - k_x u_2)]\sigma_0. \qquad (A7)$$

The $\gamma u_0 \sigma_0$ term describes the on-site energy correction due to strain, which causes an energy offset in the conduction-band minimum. The $\epsilon\delta(k_x u_2 - k_y u_1)$ term results from the correction to the bonding strengths due to modified interatomic distances in the strained lattice. This term explicitly breaks the C_3 symmetry, and is responsible for the nonzero Berry-curvature dipole discussed in the main text. The total Hamiltonian is

$$H_{\text{eff}} = H_0 + H_{\text{strain}}. \qquad (A8)$$

The parameters of the effective Hamiltonian can be obtained by fitting realistic band structures; these parameters are listed in Table II. Notably, because $\delta < 0$, a uniaxial strain with $u_{xx} > 0, u_{yy} = u_{xy} = 0$ causes a shift of the band minimum at $+K$ $(-K)$ to the left (right), which is consistent with our discussions in the main text. Also, because $\gamma < 0$, the energy offset due to strain is negative for $u_{xx} > 0$. When u_{xx} is increased, the conduction-band minimum becomes lower in energy, which is also consistent with the results in Fig. 3.

APPENDIX B: TIGHT-BINDING HAMILTONIAN

The tight-binding (TB) Hamiltonian for MoS$_2$ and MoSSe takes the same form, with the only difference being that the Rashba spin-orbit coupling for pristine MoS$_2$ is zero. In generic monolayer transition-metal dichalcogenides, the conduction- and valence-band edges are dominated by the d_{z^2}, d_{xy}, $d_{x^2-y^2}$ orbitals from the transition-metal atoms [26]. In the spinful Bloch basis of the d orbitals $\{|\mathbf{k}, d_{z^2}\rangle, |\mathbf{k}, d_{xy}\rangle, |\mathbf{k}, d_{x^2-y^2}\rangle\}$, the unstrained

TABLE II. Parameters of the effective Hamiltonian H_{eff}.

m^*/m_e	α_{SO}/a (meV)	β_0 (meV)	β_1/a^2 (meV)	γ (eV)	δ/a (eV)	a (Å)
0.5	0.3	-1.5	67	-4.2	-1.5	3.19

tight-binding Hamiltonian for a polar TMD up to nearest-neighbor (NN) hopping is written as

$$H_{\text{TB}}^0(\mathbf{k}) = H_{\text{NN}}(\mathbf{k}) \otimes \sigma_0 + \frac{1}{2}\lambda L_z \otimes \sigma_z$$
$$+ H_R(\mathbf{k}) + H_I^c(\mathbf{k}). \quad \text{(B1)}$$

The first term, $H_{\text{NN}}(\mathbf{k})$, represents the spin-independent terms, and the second term refers to the atomic spin-orbit coupling. $H_R(\mathbf{k})$ and $H_I^c(\mathbf{k})$ describe the Rashba and the Ising SOCs, respectively, near the conduction-band edge. The first two terms are given by [26]

$$H_{\text{NN}}(\mathbf{k}) = \begin{pmatrix} V_0 & V_1 & V_2 \\ V_1^* & V_{11} & V_{12} \\ V_2^* & V_{12}^* & V_{22} \end{pmatrix} - \mu I_{3\times 3},$$

$$L_z = \begin{pmatrix} 0 & 0 & 0 \\ 0 & 0 & -2i \\ 0 & 2i & 0 \end{pmatrix}. \quad \text{(B2)}$$

Here, μ denotes the chemical potential, and L_z is the z component of the orbital angular momentum. If we define $(\alpha, \beta) = \left(\frac{1}{2}k_x a, (\sqrt{3}/2)k_y a\right)$, V_0, V_1, V_2, V_{11}, V_{12}, and V_{22} are expressed as

$$V_0 = \epsilon_1 + 2t_0\left(2\cos\alpha\cos\beta + \cos 2\alpha\right), \quad \text{(B3)}$$

$$\text{Re}\,[V_1] = -2\sqrt{3}t_2 \sin\alpha\sin\beta, \quad \text{(B4)}$$

$$\text{Im}\,[V_1] = 2t_1 \sin\alpha\left(2\cos\alpha + \cos\beta\right), \quad \text{(B5)}$$

$$\text{Re}\,[V_2] = 2t_2\left(\cos 2\alpha - \cos\alpha\cos\beta\right), \quad \text{(B6)}$$

$$\text{Im}\,[V_2] = 2\sqrt{3}t_1 \cos\alpha\sin\beta, \quad \text{(B7)}$$

$$V_{11} = \epsilon_2 + (t_{11} + 3t_{22})\cos\alpha\cos\beta$$
$$+ 2t_{11}\cos 2\alpha, \quad \text{(B8)}$$

$$\text{Re}\,[V_{12}] = \sqrt{3}\,(t_{22} - t_{11})\sin\alpha\sin\beta, \quad \text{(B9)}$$

$$\text{Im}\,[V_{12}] = 4t_{12}\sin\alpha\left(\cos\alpha - \cos\beta\right), \quad \text{(B10)}$$

and

$$V_{22} = \epsilon_2 + (3t_{11} + t_{22})\cos\alpha\cos\beta$$
$$+ 2t_{22}\cos 2\alpha. \quad \text{(B11)}$$

The parameters for the NN tight-binding model are adapted from Ref. [26] and listed in Table III.

Next, we present the Ising and Rashba SOCs in the tight-binding model. Note that the Ising SOCs in the valence bands are readily described by $H_{\text{NN}}(\mathbf{k})$ together with the atomic spin-orbit coupling term. The Ising SOC in the conduction bands $H_I^c(\mathbf{k})$ takes the form

$$H_I^c(\mathbf{k}) = \begin{pmatrix} \beta(\mathbf{k}) & 0 & 0 \\ 0 & 0 & 0 \\ 0 & 0 & 0 \end{pmatrix} \otimes \sigma_z, \quad \text{(B12)}$$

where

$$\beta(\mathbf{k}) = -\frac{2\beta_{\text{SO}}^c}{3\sqrt{3}}[\sin(2\alpha) - 2\sin(\alpha)\cos(\beta)], \quad \text{(B13)}$$

with $\beta_{\text{SO}}^c = -1.5$ meV. The Rashba SOC $H_R(\mathbf{k})$ is written as

$$H_R(\mathbf{k}) = \begin{pmatrix} 2\alpha_0 & 0 & 0 \\ 0 & 0 & 0 \\ 0 & 0 & 0 \end{pmatrix} \otimes (f_x(\mathbf{k})\sigma_y - f_y(\mathbf{k})\sigma_x), \quad \text{(B14)}$$

where α_0 denotes the tight-binding Rashba parameter for d_{z^2} orbitals. In our tight-binding calculations, we set $\alpha_0 = 0.2$ meV for MoSSe. We note that α_0 is related to the effective Rashba strength α_{SO} in the effective model by $\alpha_{\text{SO}} = \frac{3}{2}\alpha_0 a$, where a is the lattice constant. The Rashba SOCs for the $\{d_{xy}, d_{x^2-y^2}\}$ orbitals are neglected as we are only concerned about the conduction-band minimum, which is dominated by d_{z^2} orbitals. The functions $f_x(\mathbf{k}), f_y(\mathbf{k})$ are given by

$$f_x(\mathbf{k}) = \sin(2\alpha) + \sin(\alpha)\cos(\beta),$$
$$f_y(\mathbf{k}) = \sqrt{3}\sin(\beta)\cos(\alpha). \quad \text{(B15)}$$

APPENDIX C: SYMMETRY-ALLOWED LINEAR COUPLING TO STRAIN FIELD

Considering $\{d_{z^2}, d_{xy}, d_{x^2-y^2}\}$ orbitals, the general form of the real-space tight-binding Hamiltonian is given by

$$\hat{H}(\overleftrightarrow{\mathbf{u}}) = \sum_{\mathbf{R},\mathbf{R}'}\sum_{\alpha,\beta} c_\alpha^\dagger(\mathbf{R})h_{\alpha,\beta}(\mathbf{R},\mathbf{R}',\overleftrightarrow{\mathbf{u}})c_\beta^\dagger(\mathbf{R}'), \quad \text{(C1)}$$

where $\mathbf{R}$, $\mathbf{R}'$ label the lattice sites, and α, β are the orbital and spin indices. Based on the general relation defined in Eq. (A5) in Sec. I, the matrix connecting a general pair of lattice sites $\mathbf{R}$, $\mathbf{R}'$ satisfies the following relation:

$$\hat{h}(\hat{g}\mathbf{R}, \hat{g}\mathbf{R}', \overleftrightarrow{\mathbf{u}}) = U(\hat{g})\hat{h}(\mathbf{R},\mathbf{R}',\hat{g}^{-1}\overleftrightarrow{\mathbf{u}})U^\dagger(\hat{g}). \quad \text{(C2)}$$

Note that Eq. (C2) is simply a generalization of the symmetry relations for unstrained case as studied in Ref. [26], should we enforce the condition that under $\hat{g}$ the strain-field tensor transforms inversely to $\overleftrightarrow{\mathbf{u}}' = \hat{g}^{-1}\overleftrightarrow{\mathbf{u}}$, with $u_0' = u_0$, $\{u_1', u_2'\} = \{u_1, u_2\}[D^{(E)}(\hat{g}^{-1})]^T$.

Under the weak applied strains considered in this paper, it is reasonable to assume that the corrections due to strain are essentially given by a linear-order coupling to the strain-field components in $\overleftrightarrow{\mathbf{u}}$. In particular, the on-site terms are invariant under the generalized transformation in Eq. (C2), which take the following form:

$$
\hat{h}_0(\overleftrightarrow{\mathbf{u}}) = (u_{xx} + u_{yy})\begin{pmatrix} E_0^S & 0 & 0 \\ 0 & E_2^S & 0 \\ 0 & 0 & E_2^S \end{pmatrix}
$$

$$
+ 2u_{xy}\begin{pmatrix} 0 & h_1^S & 0 \\ h_1^S & 0 & h_2^S \\ 0 & h_2^S & 0 \end{pmatrix}
$$

$$
+ (u_{xx} - u_{yy})\begin{pmatrix} 0 & 0 & h_1^S \\ 0 & h_2^S & 0 \\ h_1^S & 0 & -h_2^S \end{pmatrix}. \quad (C3)
$$

Next, let us consider nearest-neighbor terms. According to Eq. (C2), given the hopping term $\hat{h}(\boldsymbol{\delta}, \overleftrightarrow{\mathbf{u}})$ along a certain bonding vector $\boldsymbol{\delta} = \mathbf{R} - \mathbf{R}'$, the hopping Hamiltonian along the transformed bonding vector $\boldsymbol{\delta}' = \hat{g}\boldsymbol{\delta}$ can be explicitly given as

$$
\hat{h}(\boldsymbol{\delta}', \overleftrightarrow{\mathbf{u}}) = U(\hat{g})\hat{h}(\boldsymbol{\delta}, \hat{g}^{-1}\overleftrightarrow{\mathbf{u}})U^\dagger(\hat{g}) \quad (C4)
$$

Thus, with a knowledge of the hopping Hamiltonian $\hat{h}(\boldsymbol{\delta}, \overleftrightarrow{\mathbf{u}})$ along $\boldsymbol{\delta}$, hopping terms along all bonding vectors $\boldsymbol{\delta}' = \hat{g}\boldsymbol{\delta}$ can be obtained by acting with $\hat{g}$'s on $\hat{h}(\boldsymbol{\delta}, \overleftrightarrow{\mathbf{u}})$. The symmetry-allowed form for $\hat{h}(\boldsymbol{\delta}_1 \equiv a\hat{x}, \overleftrightarrow{\mathbf{u}})$ is given by [36]

$$
\hat{h}(\boldsymbol{\delta}_1, \overleftrightarrow{\mathbf{u}}) = u_0\hat{P}^{(A_1)} + u_1\hat{N}^{(E)} + u_2\hat{P}^{(E)}
$$

$$
= (u_{xx} + u_{yy})\begin{pmatrix} P_{00}^{(A_1)} & P_{01}^{(A_1)} & P_{02}^{(A_1)} \\ -P_{01}^{(A_1)} & P_{11}^{(A_1)} & P_{12}^{(A_1)} \\ P_{02}^{(A_1)} & -P_{12}^{(A_1)} & P_{22}^{(A_1)} \end{pmatrix}
$$

$$
+ (u_{xx} - u_{yy})\begin{pmatrix} P_{00}^{(E)} & P_{01}^{(E)} & P_{02}^{(E)} \\ -P_{01}^{(E)} & P_{11}^{(E)} & P_{12}^{(E)} \\ P_{02}^{(E)} & -P_{12}^{(E)} & P_{22}^{(E)} \end{pmatrix}
$$

$$
+ 2u_{xy}\begin{pmatrix} 0 & N_{01}^{(E)} & N_{02}^{(E)} \\ N_{01}^{(E)} & 0 & N_{12}^{(E)} \\ -N_{02}^{(E)} & N_{12}^{(E)} & 0 \end{pmatrix}. \quad (C5)
$$

The bonds in the direction $\boldsymbol{\delta}' = \hat{C}_{3z}\boldsymbol{\delta}$ are related to the bonds in the direction $\boldsymbol{\delta}$ by [36]

$$
\hat{h}(\boldsymbol{\delta}', \overleftrightarrow{\mathbf{u}}) = U(\hat{C}_{3z})\hat{h}(\boldsymbol{\delta}, \hat{C}_{3z}^{-1}\overleftrightarrow{\mathbf{u}})U^\dagger(\hat{C}_{3z}), \quad (C6)
$$

where

$$
U(\hat{C}_{3z}) = \begin{pmatrix} 1 & 0 & 0 \\ 0 & -\dfrac{1}{2} & -\dfrac{\sqrt{3}}{2} \\ 0 & \dfrac{\sqrt{3}}{2} & -\dfrac{1}{2} \end{pmatrix}. \quad (C7)
$$

For the transformed strain-tensor field $\overleftrightarrow{\mathbf{u}}' = \hat{C}_{3z}^{-1}\overleftrightarrow{\mathbf{u}}$, we have

$$
\begin{aligned}
u'_{xx} - u'_{yy} &= -\frac{1}{2}(u_{xx} - u_{yy}) - \frac{\sqrt{3}}{2}(2u_{xy}) \\
2u'_{xy} &= -\frac{1}{2}(2u_{xy}) + \frac{\sqrt{3}}{2}(u_{xx} - u_{yy})
\end{aligned} \quad (C8)
$$

in accord with the E-representation of C_{3v}. Now, with the general form of $\hat{h}(\boldsymbol{\delta}_1, \overleftrightarrow{\mathbf{u}})$ in Eq. (C5), we obtain the hopping terms for $\boldsymbol{\delta}_2 \equiv \hat{C}_{3z}\boldsymbol{\delta}_1$ and $\boldsymbol{\delta}_3 \equiv \hat{C}_{3z}^2\boldsymbol{\delta}_1$ using the relations above; these are given by

$$
\hat{h}(\boldsymbol{\delta}_2, \overleftrightarrow{\mathbf{u}}) = (u_{xx} + u_{yy})\begin{pmatrix} P_{00}^{(A1)} & -\frac{1}{2}P_{01}^{(A1)} - \frac{\sqrt{3}}{2}P_{02}^{(A1)} & \frac{\sqrt{3}}{2}P_{01}^{(A1)} - \frac{1}{2}P_{02}^{(A1)} \\ \frac{1}{2}P_{01}^{(A1)} - \frac{\sqrt{3}}{2}P_{02}^{(A1)} & \frac{1}{4}P_{11}^{(A1)} + \frac{3}{4}P_{22}^{(A1)} & P_{12}^{(A1)} + \frac{\sqrt{3}}{4}(P_{22}^{(A1)} - P_{11}^{(A1)}) \\ -\frac{\sqrt{3}}{2}P_{01}^{(A1)} - \frac{1}{2}P_{02}^{(A1)} & -P_{12}^{(A1)} + \frac{\sqrt{3}}{4}(P_{22}^{(A1)} - P_{11}^{(A1)}) & \frac{3}{4}P_{11}^{(A1)} + \frac{1}{4}P_{22}^{(A1)} \end{pmatrix}
$$

$$
+ \left[-\frac{\sqrt{3}}{2}(2u_{xy}) - \frac{1}{2}(u_{xx} - u_{yy})\right]\begin{pmatrix} P_{00}^{(E)} & -\frac{1}{2}P_{01}^{(E)} - \frac{\sqrt{3}}{2}P_{02}^{(E)} & \frac{\sqrt{3}}{2}P_{01}^{(E)} - \frac{1}{2}P_{02}^{(E)} \\ \frac{1}{2}P_{01}^{(E)} - \frac{\sqrt{3}}{2}P_{02}^{(E)} & \frac{1}{4}P_{11}^{(E)} + \frac{3}{4}P_{22}^{(E)} & P_{12}^{(E)} + \frac{\sqrt{3}}{4}(P_{22}^{(E)} - P_{11}^{(E)}) \\ -\frac{\sqrt{3}}{2}P_{01}^{(E)} - \frac{1}{2}P_{02}^{(E)} & -P_{12}^{(E)} + \frac{\sqrt{3}}{4}(P_{22}^{(E)} - P_{11}^{(E)}) & \frac{3}{4}P_{11}^{(E)} + \frac{1}{4}P_{22}^{(E)} \end{pmatrix}
$$

$$+ \left[-\frac{1}{2}(2u_{xy}) + \frac{\sqrt{3}}{2}(u_{xx} - u_{yy}) \right] \begin{pmatrix} 0 & -\frac{1}{2}N_{01}^{(E)} - \frac{\sqrt{3}}{2}N_{02}^{(E)} & \frac{\sqrt{3}}{2}N_{01}^{(E)} - \frac{1}{2}N_{02}^{(E)} \\ -\frac{1}{2}N_{01}^{(E)} + \frac{\sqrt{3}}{2}N_{02}^{(E)} & \frac{\sqrt{3}}{2}N_{12}^{(E)} & -\frac{1}{2}N_{12}^{(E)} \\ \frac{\sqrt{3}}{2}N_{01}^{(E)} + \frac{1}{2}N_{02}^{(E)} & -\frac{1}{2}N_{12}^{(E)} & -\frac{\sqrt{3}}{2}N_{12}^{(E)} \end{pmatrix}, \tag{C9}$$

$$\hat{h}(\boldsymbol{\delta}_3, \overleftrightarrow{\mathbf{u}}) = (u_{xx} + u_{yy}) \begin{pmatrix} P_{00}^{(A1)} & -\frac{1}{2}P_{01}^{(A1)} + \frac{\sqrt{3}}{2}P_{02}^{(A1)} & -\frac{\sqrt{3}}{2}P_{01}^{(A1)} - \frac{1}{2}P_{02}^{(A1)} \\ \frac{1}{2}P_{01}^{(A1)} + \frac{\sqrt{3}}{2}P_{02}^{(A1)} & \frac{1}{4}P_{11}^{(A1)} + \frac{3}{4}P_{22}^{(A1)} & P_{12}^{(A1)} - \frac{\sqrt{3}}{4}(P_{22}^{(A1)} - P_{11}^{(A1)}) \\ \frac{\sqrt{3}}{2}P_{01}^{(A1)} - \frac{1}{2}P_{02}^{(A1)} & -P_{12}^{(A1)} - \frac{\sqrt{3}}{4}(P_{22}^{(A1)} - P_{11}^{(A1)}) & \frac{3}{4}P_{11}^{(A1)} + \frac{1}{4}P_{22}^{(A1)} \end{pmatrix}$$

$$+ \left[\frac{\sqrt{3}}{2}(2u_{xy}) - \frac{1}{2}(u_{xx} - u_{yy}) \right] \begin{pmatrix} P_{00}^{(E)} & -\frac{1}{2}P_{01}^{(E)} + \frac{\sqrt{3}}{2}P_{02}^{(E)} & -\frac{\sqrt{3}}{2}P_{01}^{(E)} - \frac{1}{2}P_{02}^{(E)} \\ \frac{1}{2}P_{01}^{(E)} + \frac{\sqrt{3}}{2}P_{02}^{(E)} & \frac{1}{4}P_{11}^{(E)} + \frac{3}{4}P_{22}^{(E)} & P_{12}^{(E)} - \frac{\sqrt{3}}{4}(P_{22}^{(E)} - P_{11}^{(E)}) \\ \frac{\sqrt{3}}{2}P_{01}^{(E)} - \frac{1}{2}P_{02}^{(E)} & -P_{12}^{(E)} - \frac{\sqrt{3}}{4}(P_{22}^{(E)} - P_{11}^{(E)}) & \frac{3}{4}P_{11}^{(E)} + \frac{1}{4}P_{22}^{(E)} \end{pmatrix}$$

$$+ \left[-\frac{1}{2}(2u_{xy}) - \frac{\sqrt{3}}{2}(u_{xx} - u_{yy}) \right] \begin{pmatrix} 0 & -\frac{1}{2}N_{01}^{(E)} + \frac{\sqrt{3}}{2}N_{02}^{(E)} & -\frac{\sqrt{3}}{2}N_{01}^{(E)} - \frac{1}{2}N_{02}^{(E)} \\ -\frac{1}{2}N_{01}^{(E)} - \frac{\sqrt{3}}{2}N_{02}^{(E)} & -\frac{\sqrt{3}}{2}N_{12}^{(E)} & -\frac{1}{2}N_{12}^{(E)} \\ -\frac{\sqrt{3}}{2}N_{01}^{(E)} + \frac{1}{2}N_{02}^{(E)} & -\frac{1}{2}N_{12}^{(E)} & \frac{\sqrt{3}}{2}N_{12}^{(E)} \end{pmatrix}. \tag{C10}$$

The Hermitian property of H implies that $h(\boldsymbol{\delta}, \overleftrightarrow{\mathbf{u}}) = h^{\dagger}(-\boldsymbol{\delta}, \overleftrightarrow{\mathbf{u}})$, and thus the rest of the hopping terms in $-\boldsymbol{\delta}_i (i = 1, 2, 3)$ can simply be obtained by Hermitian conjugation. With the hopping terms along all bonding vectors above, we Fourier transform the Wannier operators:

$$\hat{c}_{\alpha}^{\dagger}(\mathbf{R}) = \frac{1}{\sqrt{N}} \sum_{\mathbf{k}} e^{-i\mathbf{k}\cdot\mathbf{R}} \hat{c}_{\mathbf{k}\alpha}^{\dagger}. \tag{C11}$$

The hopping terms in momentum space become

$$h_1(\mathbf{k}, \overleftrightarrow{\mathbf{u}}) = \sum_{n=1}^{3} e^{-i\mathbf{k}\cdot\boldsymbol{\delta}_n} \hat{h}(\boldsymbol{\delta}_n, \overleftrightarrow{\mathbf{u}}) + \text{H.c.} \tag{C12}$$

The strained momentum-space Hamiltonian can be obtained as

$$H_{\text{TB}}^{S}(\mathbf{k}) = h_0(\overleftrightarrow{\mathbf{u}}) \otimes \sigma_0 + h_1(\mathbf{k}, \overleftrightarrow{\mathbf{u}}) \otimes \sigma_0. \tag{C13}$$

Thus, the total tight-binding Hamiltonian for a strained $2H$ TMD is given by

$$H_{\text{TB}}(\mathbf{k}) = H_{\text{TB}}^{0}(\mathbf{k}) + H_{\text{TB}}^{S}(\mathbf{k}). \tag{C14}$$

The model parameters for $H_{\text{TB}}(\mathbf{k})$ used in calculating Figs. 2 and 3 are presented in Table III (unstrained parameters) and Table IV (strained parameters).

APPENDIX D: STRONGLY ENHANCED BERRY DIPOLE DUE TO SOCs

In the main text, we mention that Ω_{spin} not only enhances the magnitude of the total Berry curvature Ω_{tot} but also results in a highly nonuniform momentum-space profile for Ω_{tot}. In this section, we discuss in detail how Ω_{spin} leads to an Ω_{tot} with a very large magnitude and a nonuniform profile, and then explain why these special properties result in a strongly enhanced Berry-curvature dipole in strained MoSSe.

First of all, we show that in the regime where large Berry dipoles emerge (where the Fermi level lies close to the band-anticrossing points), the total Berry curvature Ω_{tot} in the electron bands can be approximately given as an algebraic sum of Ω_{spin} and Ω_{orb}, i.e., $\Omega_{\text{tot}} \approx \Omega_{\text{spin}} + \Omega_{\text{orb}}$.

To demonstrate the relation $\Omega_{\text{tot}} \approx \Omega_{\text{spin}} + \Omega_{\text{orb}}$, we consider $K = (4\pi/3a, 0)$ with the physics near $-K$ followed by time-reversal symmetry. In the Bloch basis of

TABLE III. Parameters for $H_{NN}(\mathbf{k})$ for monolayer MoS_2 and $MoSe_2$, adapted from Ref. [26]. All energy parameters are in units of electronvolts.

	a (Å)	ϵ_1	ϵ_2	t_0	t_1	t_2	t_{11}	t_{12}	t_{22}	λ
MoS_2	3.190	1.046	2.104	−0.184	0.401	0.507	0.218	0.338	0.057	−0.073
$MoSe_2$	3.326	0.919	2.065	−0.188	0.317	0.456	0.211	0.290	0.130	−0.091

$|d_{c,\uparrow}\rangle, |d_{c,\downarrow}\rangle, |d_{v,\uparrow}\rangle, |d_{v,\downarrow}\rangle$, the four-band Hamiltonian near K can be written as [17,22]

$$
H_{\text{tot}}(\mathbf{k}) = \begin{pmatrix}
\frac{\Delta}{2} + (\beta_0 + \beta_1' k^2) & -i\alpha_{\text{SO}}(k_x + ik_y) & V_F(k_x - ik_y) & 0 \\
i\alpha_{\text{SO}}(k_x - ik_y) & \frac{\Delta}{2} - (\beta_0 + \beta_1' k^2) & 0 & V_F(k_x - ik_y) \\
V_F(k_x + ik_y) & 0 & -\frac{\Delta}{2} + \lambda & 0 \\
0 & V_F(k_x + ik_y) & 0 & -\frac{\Delta}{2} - \lambda
\end{pmatrix}.
\tag{D1}
$$

Here, $|d_{c,\alpha}\rangle \equiv |d_{z^2}, \alpha\rangle$ denotes the predominant $|d_{z^2}\rangle$ orbital with spin $\alpha = \uparrow, \downarrow$ at the conduction-band edge at K, and $|d_{v,\alpha}\rangle \equiv |d_{x^2-y^2} + id_{xy}, \alpha\rangle$ denotes the predominant $|d_{x^2-y^2} + id_{xy}\rangle$ orbital with spin $\alpha = \uparrow, \downarrow$ at the valence-band edge at K. $V_F = 3.5$ eV· Å is the effective interorbital hopping parameter, $\Delta = 1.66$ eV is the band gap at K, and $\lambda \approx 50$ meV describes the strength of the Ising SOC in the valence band. The parameters $\beta_0, \alpha_{\text{SO}}$ are defined in the same way as in the main text. However, β_1' is not to be identified with β_1 in Eqs. (1) and (2). The relation between β_1 and the parameters $\beta_1', V_F, \Delta, \lambda$ will become clear in the following discussion.

Without loss of generality, we demonstrate the case of the lower SOC-split conduction band (band index $n = c, -$). The analysis for the upper SOC-split conduction band ($n = c, +$) is similar. For any momentum $\mathbf{k}$ displaced from K, the *exact* form of the total Berry curvature in the lower conduction band is given by

$$\Omega_{c,-}^{\text{tot}}(\mathbf{k}) = \Omega_{c,-}^{\text{inter}}(\mathbf{k}) + \Omega_{c,-}^{\text{intra}}(\mathbf{k}),$$

$$
\Omega_{c,-}^{\text{inter}}(\mathbf{k}) = i \sum_{m=\pm} \frac{\langle c, -, \mathbf{k}|\hat{v}_x|v, m, \mathbf{k}\rangle \langle v, m, \mathbf{k}|\hat{v}_y|c, -, \mathbf{k}\rangle - \text{c.c.}}{[E_{c,-}(\mathbf{k}) - E_{v,m}(\mathbf{k})]^2},
$$

$$
\Omega_{c,-}^{\text{intra}}(\mathbf{k}) = i \frac{\langle c, -, \mathbf{k}|\hat{v}_x|c, +, \mathbf{k}\rangle \langle c, +, \mathbf{k}|\hat{v}_y|c, -, \mathbf{k}\rangle - \text{c.c.}}{[E_{c,-}(\mathbf{k}) - E_{c,+}(\mathbf{k})]^2}.
\tag{D2}
$$

Here, $n = c$ (v), $+$ ($-$) is the band index for the Bloch eigenstate $|n, \mathbf{k}\rangle$ of $H_{\text{tot}}(\mathbf{k})$, associated with a band energy $E_n(\mathbf{k})$; $+$ ($-$) labels the upper (lower) SOC-split band; and c (v) labels the conduction (valence) band. $\hat{v}_i \equiv \partial H_{\text{tot}}/\partial k_i$, with $i = x, y$, is the velocity operator in the i direction.

As shown in Ref. [22], at exactly the K-point ($\mathbf{k} = 0$), the Ω^{inter} term in the second line of Eq. (D2) arises from interband coupling between the conduction and valence bands. It reduces to the orbital-type Berry curvature Ω_{orb}. The Ω^{intra} term in the third line of Eq. (D2) arises from intraband coupling between the two conduction bands which are split by SOCs. It reduces to the spin-type Berry curvature Ω_{spin} at exactly the K-point. Thus, $\Omega_{\text{tot}} = \Omega_{\text{spin}} + \Omega_{\text{orb}}$ holds strictly at the K-point. It was also

TABLE IV. Strained tight-binding parameters up to nearest-neighbor hopping terms for monolayer MoS_2 and $MoSe_2$, adapted from Ref. [36]. All parameters are in units of electronvolts.

	MoS_2						$MoSe_2$					
On-site	E_0^S	E_2^S	h_1^S	h_2^S			E_0^S	E_2^S	h_1^S	h_2^S		
	−1.021	−1.817	−0.043	−0.370			−1.090	−2.023	0.004	−0.296		
NN	$P_{00}^{(A1)}$	$P_{01}^{(A1)}$	$P_{02}^{(A1)}$	$P_{11}^{(A1)}$	$P_{12}^{(A1)}$	$P_{22}^{(A1)}$	$P_{00}^{(A1)}$	$P_{01}^{(A1)}$	$P_{02}^{(A1)}$	$P_{11}^{(A1)}$	$P_{12}^{(A1)}$	$P_{22}^{(A1)}$
	1.032	−0.285	−0.738	−1.027	0.206	1.544	0.885	−0.236	−0.596	−0.951	0.195	1.333
	$P_{00}^{(E)}$	$P_{01}^{(E)}$	$P_{02}^{(E)}$	$P_{11}^{(E)}$	$P_{12}^{(E)}$	$P_{22}^{(E)}$	$P_{00}^{(E)}$	$P_{01}^{(E)}$	$P_{02}^{(E)}$	$P_{11}^{(E)}$	$P_{12}^{(E)}$	$P_{22}^{(E)}$
	0.376	−0.188	−0.779	−0.910	−0.003	1.337	0.333	−0.126	−0.667	−0.793	0.008	1.108
	$N_{01}^{(E)}$	$N_{02}^{(E)}$	$N_{12}^{(E)}$				$N_{01}^{(E)}$	$N_{02}^{(E)}$	$N_{12}^{(E)}$			
	0.288	0.152	−0.634				0.255	0.110	−0.565			

pointed out in Ref. [22] that, based on the symmetry property of the Berry curvature around C_3-invariant K-points, $\Omega_{tot} \approx \Omega_{spin} + \Omega_{orb}$ holds in the close vicinity of K.

Now, we show that throughout the Fermi-level regime considered in this paper, $\Omega^{intra} \approx \Omega_{spin}$ and $\Omega^{inter} \approx \Omega_{orb}$ hold. As a result, we have $\Omega_{tot} \approx \Omega_{spin} + \Omega_{orb}$. To see why $\Omega^{intra} \approx \Omega_{spin}$, we note that at a finite momentum $\mathbf{k}$, the weight of the $|d_v\rangle \equiv |d_{x^2-y^2} + id_{xy}\rangle$ states in the eigenstates $|c, \pm, \mathbf{k}\rangle$ of the conduction bands is of order $w_v \sim V_F^2 k^2/\Delta^2$ according to perturbation theory. As the relevant Fermi level ranges from 0 to 30 meV measured from the conduction-band minimum, the relevant momentum range covers $0 \text{ Å}^{-1} < k < 0.06 \text{ Å}^{-1}$, measured from $K = 1.31 \text{ Å}^{-1}$ (Fig. 4). With $V_F = 3.5$ eV·Å and $\Delta = 1.66$ eV, the weight of the $|d_{x^2-y^2} + id_{xy}\rangle$ state is $w_v < 2\%$ throughout this range. This suggests that in all ranges of Fermi level studied in this paper, the electronic states in the conduction band are strongly dominated by the $|d_c\rangle \equiv |d_{z^2}\rangle$ orbitals.

The negligible contribution from $|d_{x^2-y^2} + id_{xy}\rangle$ states in the electronic wave functions allows us to construct an effective two-band Hamiltonian $H_{eff}(\mathbf{k})$ formed by $\{|d_{z^2}, \uparrow\rangle, |d_{z^2}, \downarrow\rangle\}$ states for conduction-band electrons within the range $0 \text{ Å}^{-1} < k < 0.06 \text{ Å}^{-1}$, such that the eigenstates $|d_{z^2}, \pm\rangle$ together with their corresponding eigenvalues $E_\pm(\mathbf{k})$ of $H_{eff}(\mathbf{k})$ are perturbatively good approximations to $|c, \pm, \mathbf{k}\rangle$ and $E_{c,\pm}(\mathbf{k})$ for evaluating Ω^{intra} in Eq. (D2).

In fact, such an effective model can be obtained by treating the intra-$|d_{z^2}\rangle$-orbital terms in $H_{tot}(\mathbf{k})$ [Eq. (D1)] as an unperturbed Hamiltonian, while the coupling between $|d_{z^2}\rangle$ and the remote $|d_{x^2-y^2} + id_{xy}\rangle$ states (which are predominantly in the valence band) in Eq. (D1) are regarded as perturbations. Based on generalized second-order perturbation theory, we project the contributions from the $|d_{x^2-y^2} + id_{xy}\rangle$ states onto the subspace of $\{|d_{z^2}, \uparrow\rangle, |d_{z^2}, \downarrow\rangle\}$ states and obtain the effective two-band Hamiltonian (for $k \sim 0$–0.06 Å^{-1})

$$H_{eff}(\mathbf{k}) = \left(\frac{\Delta V_F^2}{\Delta^2 - \lambda^2} k^2\right)\sigma_0 + \alpha_{SO}\mathbf{k} \times \boldsymbol{\sigma}_\parallel$$
$$+ \left(\beta_0 + \beta_1' k^2 + \frac{\lambda V_F^2}{\Delta^2 - \lambda^2} k^2\right)\sigma_z. \quad \text{(D3)}$$

Here, the Pauli matrices σ act on the spins of d_{z^2} orbitals, and $k^2 = k_x^2 + k_y^2$. For simplicity, we drop all constant terms in Eq. (D3) which have no contributions to Berry curvatures. Notably, the form of H_{eff} in Eq. (D3) is exactly the same as that of H_0 [Eq. (1)], which is derived based on the C_{3v} point-group symmetry. In particular, by defining $\beta_1 \equiv \beta_1' + \lambda V_F^2/(\Delta^2 - \lambda^2)$, we identify the σ_z term in H_{eff} as exactly the Ising SOC term discussed in Eq. (1).

Thus, the Berry curvature derived from H_{eff}, which serves as a perturbative approximation to Ω^{intra}, is exactly the spin-type Berry curvature Ω_{spin} discussed in the main text. Therefore, we conclude that $\Omega^{intra}(\mathbf{k}) \approx \Omega_{spin}(\mathbf{k})$ throughout the regime explored in this paper.

Next, we show that $\Omega^{inter} \approx \Omega_{orb}$ is also true for $k \sim 0$–0.06 Å^{-1}. By the same reasoning as above, it is straightforward to see that the weight of the $|d_{z^2}\rangle$ orbitals in the valence-band states is also on the order of $V_F^2 k^2/\Delta^2 < 2\%$ within the range $k \sim 0$–0.06 Å^{-1}. Thus, to evaluate the interband contribution Ω^{inter}, the eigenstates $|c, -, \mathbf{k}\rangle$ and $|v, \pm, \mathbf{k}\rangle$ can be well approximated as $|c, -, \mathbf{k}\rangle \approx |d_{z^2}, -, \mathbf{k}\rangle$ and $|v, \pm, \mathbf{k}\rangle \approx |d_{x^2-y^2} + id_{xy}, \pm, \mathbf{k}\rangle$. We note that, due to the Rashba SOCs, the out-of-plane spin of the eigenstates in the conduction band is no longer conserved. Thus, we have in general $|d_{z^2}, -, \mathbf{k}\rangle = s_1(\mathbf{k})|d_{z^2}, \uparrow\rangle + s_2(\mathbf{k})|d_{z^2}, \downarrow\rangle$, and the $\mathbf{k}$-dependent coefficients s_1, s_2 need to be determined by diagonalizing $H_{eff}(\mathbf{k})$. However, by observing that $\Delta \gg \lambda \gg \beta_0, \beta_1 k^2$ in the regime of interest, we have $E_{c,-}(\mathbf{k}) - E_{v,\pm}(\mathbf{k}) \approx \Delta$. With $|d_{x^2-y^2} + id_{xy}, +(-), \mathbf{k}\rangle = |d_{x^2-y^2} + id_{xy}, \uparrow(\downarrow), \mathbf{k}\rangle$, we have

$$\Omega^{inter}_{c,-}(\mathbf{k}) = i\sum_{m=\pm} \frac{\langle c, -, \mathbf{k}|\hat{v}_x|v, m, \mathbf{k}\rangle\langle v, m, \mathbf{k}|\hat{v}_y|c, -, \mathbf{k}\rangle - \text{c.c.}}{[E_{c,-}(\mathbf{k}) - E_{v,m}(\mathbf{k})]^2}$$
$$\approx -\left(|s_1(\mathbf{k})|^2 \frac{V_F^2}{\Delta^2} + |s_2(\mathbf{k})|^2 \frac{V_F^2}{\Delta^2}\right)$$
$$= -\frac{V_F^2}{\Delta^2}. \quad \text{(D4)}$$

Note that in the last step we use the normalization condition $|s_1|^2 + |s_2|^2 = 1$. As shown in Ref. [17], in the limit $V_F k \ll \Delta$, Ω_{orb} is almost a constant, with value V_F^2/Δ^2 (a uniform momentum-space profile in the neighborhood of K). It is clear that $V_F k \ll \Delta$ holds in the range $k \sim 0$–0.06 Å^{-1} of interest. Thus, we have $\Omega^{inter} \approx \Omega_{orb}$.

Based on our detailed analysis above, we conclude that $\Omega_{tot} \approx \Omega_{spin} + \Omega_{orb}$ holds throughout the regime explored in the present paper. We note that this relation would fail when $V_F k \sim \Delta$. However, this would require the Fermi level to exceed 100 meV [26], which goes way beyond the regime of interest.

According to Fig. 4, $|\Omega_{spin}| \sim 10^4 \text{ Å}^2$ near the band-anticrossing points, while $|\Omega_{orb}| \sim 10 \text{ Å}^2$ [17]. Thus, Ω_{spin} strongly dominates over Ω_{orb} near the band-anticrossing points. Based on our discussion in Sec. II A, the relation $\Omega_{tot} \approx \Omega_{spin} + \Omega_{orb}$ implies that the behavior of Ω_{tot} is essentially governed by Ω_{spin} in the regime of interest. In this section, we explicitly demonstrate how the dominance of Ω_{spin} gives rise to a strongly enhanced Berry dipole of order 1 Å near the band-anticrossing points, as shown in Figs. 2 and 3.

First, to demonstrate how Ω_{spin} significantly enhances the total Berry curvature in strained MoSSe, we plot the
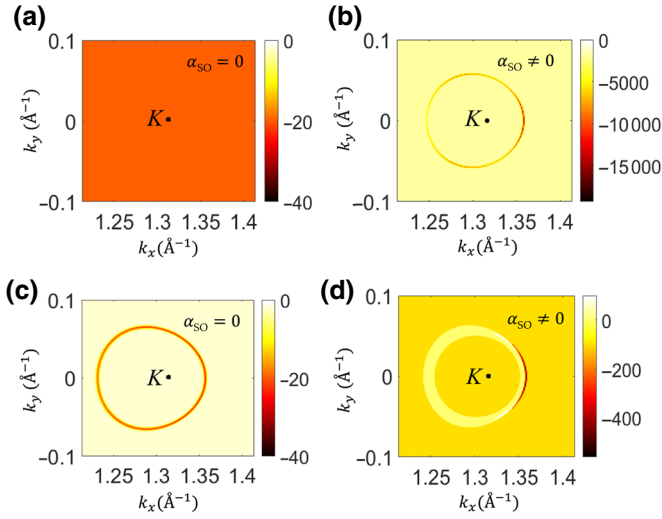
FIG. 5. Effects of Ω_{spin} on total Berry-curvature profile in strained MoSSe. The color bar indicates the value of the total Berry curvature in units of Å^2. (a),(b) Profiles of Ω_{tot} for the lower conduction band $n = c, -$ throughout the neighborhood of K in (a) strained MoS$_2$ without Ω_{spin} and (b) strained MoSSe with Ω_{spin}. (c),(d) Profiles of Ω_{tot} along the Fermi contour enclosing the K-point at $E_F = 1.467$ eV in (c) strained MoS$_2$ without Ω_{spin} and (d) strained MoSSe with Ω_{spin}.

profiles of Ω_{tot} for the lower conduction band $n = c, -$ *throughout the neighborhood of K* in Figs. 5(a) and 5(b). In Fig. 5(a), the Rashba SOC is absent ($\alpha_{\text{SO}} = 0$), and thus $\Omega_{\text{spin}} = 0$ according to Eq. 2. In this case, the magnitude of Ω_{tot} remains almost constant on the order of 10 Å^2. Notably, as discussed in Sec. II A, the profile of Ω_{tot} is approximately a uniform function near K due to the fact that $V_F k \ll \Delta$ [17].

In contrast, when the Rashba SOC is present, the maximum amplitude of Ω_{tot} is significantly enhanced near the band-anticrossing points due to the presence of Ω_{spin} [Fig. 5(b)]. Note that the magnitude of Ω_{tot} is also on the order of 10^4 Å^2, and is consistent with the relation $\Omega_{\text{tot}} \approx \Omega_{\text{spin}} + \Omega_{\text{orb}}$. Importantly, as the magnitude of Ω_{spin} changes dramatically as $\mathbf{k}$ goes from K to the band-anticrossing points [Eq. (2)], the profile of Ω_{tot} also becomes highly nonuniform in the neighborhood of K, as explicitly shown in Fig. 5(b).

Second, to demonstrate how Ω_{spin} leads to a strongly enhanced Berry dipole in strained MoSSe, we plot the Berry-curvature profiles *along a fixed Fermi contour enclosing the K-point* (i.e., only momentum states at a given Fermi energy E_F are considered), as shown in Figs. 5(c) and 5. This provides a physical picture of a Berry dipole according to Eq. (4), which can be regarded as a manifestation of its Fermi-liquid property. As shown in Fig. 5(c), when Ω_{spin} is absent, the total Berry curvature Ω_{tot} is also approximately a constant along the Fermi contour due to the uniform Berry-curvature profile throughout
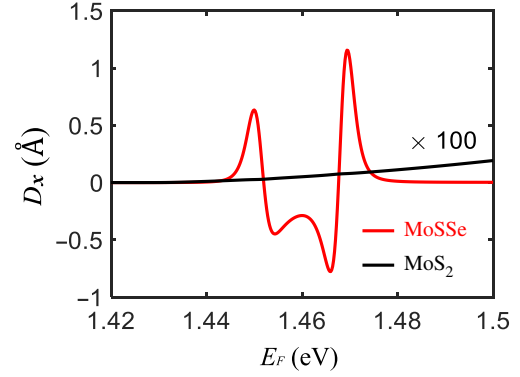

FIG. 6. Gate dependence of Berry-curvature dipole D_x in strained MoS$_2$ (black solid line) and strained MoSSe (red solid line) for $u_{xx} = 4\%$. Note that D_x in strained MoS$_2$ is multiplied by 100 times so that the values can be visible on a scale of 0.5 Å. For direct comparison, all parameters used for calculating both curves are set to be the same except that $\alpha_{\text{SO}} \neq 0$ for MoSSe.

the neighborhood of K (Fig. 5). As the Berry dipole is given by a sum of products between the Fermi velocity and the Berry curvature at each $\mathbf{k}$ along the Fermi surface [Eq. (4)], the contributions from all states $\mathbf{k}$ in Fig. 5(c) almost cancel each other because their Berry curvatures are roughly the same, while their velocities almost sum to zero.

In sharp contrast, with the same Fermi contour as in Fig. 5(c), due to the highly nonuniform profile of Ω_{tot} in Fig. 5(b), Ω_{tot} also changes drastically along the Fermi contour, as shown in Fig. 5(d). Note that due to the broken C_3 symmetry caused by the strain, the Berry-curvature profile is no longer threefold invariant about K. Particularly, with the choice of a Fermi energy lying close to the hot spots of Ω_{spin} associated with the right-movers, the Berry curvature along the Fermi contour enclosing K is concentrated preferentially on the right-hand side of K [Fig. 5(d)]. In this case, the largely unbalanced Berry-curvature contributions from right-movers and left-movers lead to a large Berry dipole according to Eq. (4).

We now explicitly demonstrate the enhancement of the Berry dipole due to Ω_{spin}. We calculate the Berry dipole for strained conventional MoS$_2$ without Rashba SOCs for a direct comparison with strained MoSSe with Rashba SOCs. As shown clearly in Fig. 6, the magnitude of D_x in MoS$_2$ is only of order 1×10^{-3} Å in the regime where D_x is of order 1 Å in strained MoSSe. Thus, D_x is strongly enhanced by 3 orders of magnitude in the Fermi-level regime $E_F \sim 1.44$–1.48 eV due to the presence of Ω_{spin}. We note in passing that the optimal value of D_x in strained MoS$_2$ (with contributions from Ω_{orb} only) can be on the order of 0.01 Å at a higher E_F which goes beyond the regime considered here. Thus, the optimal value is also enhanced by 2 orders of magnitude due to Ω_{spin}.

APPENDIX E: BERRY-CURVATURE DIPOLE IN OTHER STRAINED POLAR TMDs

Here, we discuss nonlinear Hall effects in other strained polar TMDs. First, as mentioned in the main text, our prediction of a large Berry dipole generally applies to the whole class of molybdenum-based polar TMDs. This is due to the fact that in all conventional molybdenum-based TMDs, there readily exists a band crossing within the two electron bands [26]. As a result, once the Rashba SOCs are turned on, the band-crossing points are gapped out, leading to band anticrossings where Berry-curvature hot spots can emerge.

To explicitly demonstrate the generality of the mechanism above, we calculate the gate dependence of the Berry dipole in another molybdenum-based TMD material, MoSeTe, as shown in Fig. 7(a), under a uniaxial strain $u_{xx} = 2\%$. The tight-binding model used for MoSeTe is exactly the same as the one presented in Secs. II and III, with the parameters for MoSeTe listed in Tables III and IV. The SOC tight-binding parameters for MoSeTe are given by $\alpha_0 = 1.2$ meV and $\beta_{SO} = -15$ meV. Clearly, D_x in MoSeTe has the same qualitative gate-dependent features as that in MoSSe under a similar strain $u_{xx} \sim 2\%$ (Fig. 3). Notably, the optimal value of D_x in MoSeTe is also of order 1 Å.

On the other hand, as pointed out in the main text, in tungsten-based $2H$ TMDs, the SOC-induced Berry curvature Ω_{spin} can also modify the total Berry-curvature profile near the conduction-band minimum. However, since there is no band anticrossing in W-based materials, the Berry-curvature profile is much less nonuniform tha in the molybdenum-based case and the Berry-curvature dipole is expected to be less strongly enhanced. Here, using a specific example of a W-based polar TMD candidate, WSeTe, we demonstrate this fact by calculating the Berry-curvature dipole under the same uniaxial strain $u_{xx} = 4\%$ as in Fig. 2. For W-based materials, the Ising SOC in the conduction band is set to $\beta_0 \approx 20$ meV [26]. A strong Rashba splitting on the order of 50 meV has also been predicted for WSeTe [20], and the fitted parameter in the tight-binding model is set to $\alpha_0 \approx 45$ meV according to previous studies [22]. For
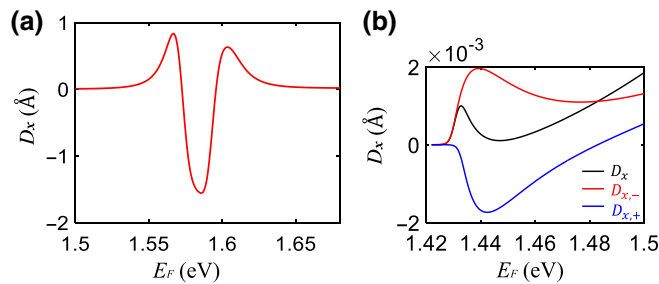
simplicity, the other parameters are set to the same values as those presented in Tables III and IV.

The Berry-curvature dipole D_x is shown as a function of the Fermi energy E_F for strained WSeTe in Fig. 7(b). Clearly, the Berry-curvature dipole is also on the order of 1×10^{-3} Å, comparable to the case of conventional $2H$ TMDs, while it is much smaller than the values in strained MoSSe (Fig. 2). However, because Ω_{spin} causes the two bands to carry opposite Berry curvatures, the contributions $D_{x,-}$ and $D_{x,+}$ from the lower and upper bands, respectively, to D_x also have different signs, as shown in Fig. 7(b), which results in some cancellation effects as the upper band becomes filled (signified by the point in the D_x-E_F curves where D_x starts to deviate from $D_{x,-}$). While a certain nontrivial gate dependence is also found in D_x, the sign of D_x is not switched as in the case of MoSSe (Figs. 2 and 3).

---

[1] D. Xiao, M. Chang, and Q. Niu, Berry phase effects on electronic properties, Rev. Mod. Phys. **82**, 1959 (2010).

[2] Naoto Nagaosa, Jairo Sinova, Shigeki Onoda, A. H. MacDonald, and N. P. Ong, Anomalous Hall effect, Rev. Mod. Phys. **82**, 1539 (2010).

[3] L. D. Landau, E. M. Lifshitz, and L. P. Pitaevskii, in *Statistical Physics*, Course of Theoretical Physics Vol. 5 (Pergamon Press, Oxford, 1999), 3rd ed.

[4] Dimitrie Culcer, Allan MacDonald, and Qian Niu, Anomalous Hall effect in paramagnetic two-dimensional systems, Phys. Rev. B **68**, 045327 (2003).

[5] Inti Sodemann and Liang Fu, Quantum Nonlinear Hall Effect Induced by Berry Curvature Dipole in Time-Reversal Invariant Materials, Phys. Rev. Lett. **115**, 216806 (2015).

[6] J. Lee, Z. Wang, H. Xie, K. F. Mak, and J. Shan, Valley magnetoelectricity in single-layer MoS2, Nat. Mater. **16**, 887 (2017).

[7] Hiroki Isobe, Su-Yang Xu, and Liang Fu, *High-frequency rectification via chiral Bloch electrons*, arXiv:1812.08162 (2018).

[8] Tony Low, Yongjin Jiang, and Francisco Guinea, Topological currents in black phosphorus with broken inversion symmetry, Phys. Rev. B **92**, 235447 (2015).

[9] E. Deyo, L. E. Golub, E. L. Ivchenko, and B. Spivak, *Semiclassical theory of the photogalvanic effect in noncentrosymmetric systems*, arXiv:0904.1917 (2009).

[10] Lukas Muechler, A. Alexandradinata, Titus Neupert, and Roberto Car, Topological Nonsymmorphic Metals from Band Inversion, Phys. Rev. X **6**, 041069 (2016).

[11] Jhih-Shih You, Shiang Fang, Su-Yang Xu, Efthimios Kaxiras, and Tony Low, Berry curvature dipole current in the transition metal dichalcogenides family, Phys. Rev. B **98**, 121109(R) (2018).

[12] Y. Zhang, J. V. d. Brink, C. Felser, and B. Yan, Electrically tuneable nonlinear anomalous Hall effect in two-dimensional transition-metal dichalcogenides WTe2 and MoTe2, 2D Materials **5**, 044001 (2018).

[13] Qiong Maa, *et al.*, Observation of the nonlinear Hall effect under time-reversal-symmetric conditions, Nature **565**, 337 (2018).

(a) **(b)**

FIG. 7. Gate dependence of Berry-curvature dipole D_x in (a) strained MoSeTe with $u_{xx} = 2\%$ and (b) strained WSeTe with $u_{xx} = 4\%$.

[14] Kaifei Kang, Tingxin Li, Egon Sohn, Jie Shan, and Kin Fai Mak, Observation of the nonlinear anomalous Hall effect in 2D WTe$_2$, Nat. Mater. **18,** 324 (2019).

[15] Z. Z. Du, C. M. Wang, Hai-Zhou Lu, and X. C. Xie, Band Signatures for Strong Nonlinear Hall Effect in Bilayer WTe$_2$, Phys. Rev. Lett. **121,** 266601 (2018).

[16] P. Olbrich, L. E. Golub, T. Herrmann, S. N. Danilov, H. Plank, V. V. Belkov, G. Mussler, Ch. Weyrich, C. M. Schneider, J. Kampmeier, D. Grutzmacher, L. Plucinski, M. Eschbach, and S. D. Ganichev, Room-Temperature High-Frequency Transport of Dirac Fermions in Epitaxially Grown Sb$_2$Te$_3$- and Bi$_2$Te$_3$-Based Topological Insulators, Phys. Rev. Lett. **113,** 096601 (2014).

[17] D. Xiao, G. Liu, W. Feng, X. Xu, and W. Yao, Coupled Spin and Valley Physics in Monolayers of MoS$_2$ and Other group-VI Dichalcogenides, Phys. Rev. Lett. **108,** 196802 (2012).

[18] K. F. Mak, K. L. McGill, J. Park, and P. L. McEuen, The valley Hall effect in MoS2 transistors Science **344,** 1489 (2014).

[19] J. M. Lu, O. Zheliuk, I. Leermakers, N. F. Q. Yuan, U. Zeitler, K. T. Law, and J. T. Ye, Evidence for two-dimensional Ising superconductivity in gated MoS$_2$, Science **350,** 1353 (2015).

[20] Qun-Fang Yao, Jia Cai, Wen-Yi Tong, Shi-Jing Gong, Ji-Qing Wang, Xiangang Wan, Chun-Gang Duan, and J. H. Chu, Manipulation of the large Rashba spin splitting in polar two-dimensional transition-metal dichalcogenides, Phys. Rev. B **95,** 165401 (2017).

[21] Y. C. Cheng, Z. Y. Zhu, M. Tahir, and U. Schwingenschlogl, Spin-orbit-induced spin splittings in polar transition metal dichalcogenide monolayers, Europhys. Lett. **102,** 57001 (2013).

[22] Benjamin T. Zhou, Katsuhisa Taguchi, Yuki Kawaguchi, Yukio Tanaka, and K. T. Law, Spin-orbit-coupling induced valley Hall effects in transition-metal dichalcogenides, Communications Physics **2,** 26 (2019).

[23] K. Taguchi, B. T. Zhou, Y. Kawaguchi, Y. Tanaka, and K. T. Law, Valley Edelstein effect in monolayer transition-metal dichalcogenides, Phys. Rev. B **98,** 035435 (2018).

[24] Ang-Yu Lu, Hanyu Zhu, Jun Xiao, Chih-Piao Chuu, Yimo Han, Ming-Hui Chiu, Chia-Chin Cheng, Chih-Wen Yang, Kung-Hwa Wei, Yiming Yang, Yuan Wang, Dimosthenis Sokaras, Dennis Nordlund, Peidong Yang, David A. Muller, Mei-Yin Chou, Xiang Zhang, and Lain-Jong Li, Janus monolayers of transition metal dichalcogenides, Nat. Nanotech. **12,** 744 (2017).

[25] Jing Zhang, Shuai Jia, Iskandar Kholmanov, Liang Dong, Dequan Er Weibing Chen, Hua Guo, Zehua Jin, Vivek B. Shenoy, Li Shi, and Jun Lou, Janus monolayer transition-metal dichalcogenides, ACS Nano **8,** 8192 (2017).

[26] G.-B. Liu, W.-Y. Shan, Y. Yao, W. Yao, and D. Xiao, Three-band tight-binding model for monolayers of group-VIB transition metal dichalcogenides, Phys. Rev. B **88,** 085433 (2013).

[27] N. F. Q. Yuan, K. F. Mak, and K. T. Law, Possible Topological Superconducting Phases of MoS$_2$, Phys. Rev. Lett. **113,** 097001 (2014).

[28] H. T. Yuan, Mohammad Saeed Bahramy, Kazuhiro Morimoto, Sanfeng Wu, Kentaro Nomura, Bohm-Jung Yang, Hidekazu Shimotani, Ryuji Suzuki, Minglin Toh, Christian Kloc, Xiaodong Xu, Ryotaro Arita, Naoto Nagaosa, and Yoshihiro Iwasa, Zeeman-type spin splitting controlled by an electric field, Nat. Phys. **9,** 563 (2013).

[29] Z. Y. Zhu, Y. C. Cheng, and U. Schwingenschlogl, Giant spin-orbit-induced spin splitting in two-dimensional transition-metal dichalcogenide semiconductors, Phys. Rev. B **84,** 153402 (2011).

[30] A. Kormanyos, V. Zolyomi, N. D. Drummond, P. Rakyta, G. Burkard, and V. I. Falko, Monolayer MoS$_2$: Trigonal warping, the Γ valley, and spin-orbit coupling effects, Phys. Rev. B **88,** 045416 (2013).

[31] K. Kośmider, J. W. González, and J. Fernández-Rossier, Large spin splitting in the conduction band of transition metal dichalcogenide monolayers, Phys. Rev. B **88,** 245436 (2013).

[32] E. I. Rashba, Symmetry of bands in Wurzite-type crystals. 1. Symmetry of bands disregarding spin-orbit interaction, Sov. Phys. Solid. State **1,** 368 (1959).

[33] B. Andrei Bernevig, Taylor L. Hughes, and Shou-Cheng Zhang, Quantum spin Hall effect and topological phase transition in HgTe Quantum wells, Science **314,** 5806 (2006).

[34] X. L. Qi, Y. S. Wu, and S. C. Zhang, General theorem relating the bulk topological number to edge states in two-dimensional insulators, Phys. Rev. B **74,** 045125 (2006).

[35] G. E. Volovik, *The Universe in a Helium Droplet* (Oxford University Press, USA, 2003).

[36] Shiang Fang, Stephen Carr, Miguel A. Cazalilla, and Efthimios Kaxiras, Electronic structure theory of strained two-dimensional materials with hexagonal symmetry, Phys. Rev. B **98,** 075106 (2018).

[37] S. Hemour and K. Wu, Radio-frequency rectifier for electromagnetic energy harvesting: development path and future outlook, Proc. IEEE **102,** 1667 (2014).

[38] K. V. Selvan and M. S. Mohamed Ali, Micro-scale energy harvesting devices: Review of methodological performances in the last decade, Renew. Sust. Energ. Rev. **54,** 1035 (2016).

[39] Jieun Lee, Kin Fai Mak, and Jie Shan, Electrical control of the valley Hall effect in bilayer MoS2 transistors, Nat. Nanotech. **11,** 421 (2016).

[40] Zefei Wu, Benjamin T. Zhou, Xiangbin Cai, Patrick Cheung, Gui-Bin Liu, Meizhen Huang, Jiangxiazi Lin, Tianyi Han, Liheng An, Yuanwei Wang, Shuigang Xu, Gen Long, Chun Cheng, Kam Tuen Law, Fan Zhang, and Ning Wang, Intrinsic valley Hall transport in atomically thin MoS$_2$, Nat. Commun. **10,** 611 (2019).

[41] E. J. König, M. Dzero, A. Levchenko, and D. A. Pesin, Gyrotropic hall effect in berry-curved materials, Phys. Rev. B **99,** 155404 (2019).

[42] S. Nandy and I. Sodemann, arXiv:1901.04467, (2019).

[43] Z. Z. Du, C. M. Wang, Shuai Li, Hai-Zhou Lu, and X. C. Xie, Nat. Commun. **10,** 3047 (2019).

[44] Cong Xiao, Z. Z. Du, and Qian Niu, arXiv:1907.00577, (2019).